Doctoral Dissertation

Interfacial Fluctuation and Fluid Convection in Meniscus Splitting of Polysaccharide Dispersions

Leijie WU

Supervisor: Kosuke OKEYOSHI

Division of Advanced Science and Technology

Japan Advanced Institute of Science and Technology

[Materials Science]

September 2025

Referee-in-chief: Associate Professor Dr. Kosuke OKEYOSHI

Japan Advanced Institute of Science and Technology

Referees:

Professor Dr. Masayuki YAMAGUCHI

Japan Advanced Institute of Science and Technology

Professor Dr. Yuzuru TAKAMURA

Japan Advanced Institute of Science and Technology

Associate Professor Dr. Kenta HONGO

Japan Advanced Institute of Science and Technology

External referee:

Professor Dr. Takashi MIYATA

Kansai University

Abstract

Splitting patterns in nature, such as geometric patterns of Salt Lake, wrinkles patterns of hydrogels, and Rayleigh–Bénard patterns in heated fluids, are not randomly generated, but rather are self-organizing in nonequilibrium systems. Closely related to the dissipative structures, the evolution from disorder to ordered patterning through continuous exchange of energy and matter in open systems. This thesis focuses on the meniscus splitting patterns in drying polysaccharides dispersion systems and aims at exploring the kinetic mechanism both on the interfacial behavior and inter-fluid behaviors during the evaporation process, specifically. In Chapter 2, the recognition of spatial finiteness in "meniscus splitting phenomena" in aqueous polymer dispersions is demonstrated during water evaporation. By providing heat energy to polymer dispersions in a Hele-Shaw cell, an interface fluctuation with concentration unevenness is induced to split the evaporative interface. The results of the quasi-natural experiments revealed that the nonequilibrium drying period for repositioning polymer clusters allows for considerable changes in Reynolds number in a low range ($<10^{-6}$) to form multiple nuclei, like the life in living organisms. In Chapter 3, by studying the internal flow during nonequilibrium process, the evolution of unique mass flows as Marangoni circulations is demonstrated during the growth of splitting pattern. The confluences of multiple circulations are distinctly aligned one-to-one with the nucleation positions. This convection patterns periodically integrates the polymers in a quasi-two-dimensional space. By studying the Marangoni convection in different capillary environments, the disappearance of convection implies a different role of capillary forces and surface tension. In Chapter 4, we investigate how evaporation-induced convection influence interfacial fluctuations and nucleation behavior in meniscus splitting. Using pectin dispersion, we compared the synchronous and asynchronous nucleation process. Through introducing the asymmetry bottoms (flat, step-like, sloped) to break convective symmetry, confirmed the influence of spatial symmetry on convective nucleation. Furthermore, we

compare pectin and xanthan gum dispersions, which exhibit dramatically different flow behaviors under evaporation: Marangoni circulations in the former, and almost no internal flow in the latter. From the emergence of convection to interfacial fluctuations and flocculation-induced nucleation, the hydrodynamic mechanism in meniscus splitting offers new insights into the evaporation induced self-assembly of polymer dispersion/colloidal. This has significant implications for understanding pattern formation in nature, particularly interfacial structures in biopolymer and soft matter systems spanning micro to macroscopic scales.

Keywords: Dissipative structures, Fluctuations, Polysaccharides, Skin layer, Marangoni effect, Capillary effect.

Acknowledgements

First and foremost, I wish to express my sincere appreciation to my advisor, Professor Okeyoshi, for your unwavering guidance, insightful wisdom, and constant encouragement throughout these years. Your rigorous attitude toward research and your meticulous care for your students have left a lasting impression on me. Under your mentorship, I have not only grown as a researcher but also as a person. As the Chinese saying goes, “once a teacher, always a mentor for life”. I would also emphasize my gratitude to Prof. Yamahuchi Masayuki, and Prof. Hongo Kenta, as well as the professors and researchers I met in The Society of Polymer Science, Japan (SPSJ) and The Research Group on Polymer Gels.

To my beloved parents and family, though separated by thousands of miles, your emotional support and quiet strength have always been with me. Your selfless love is like the steady flow of a river — gentle, enduring, and powerful. Thank you for being the solid ground upon which I could stand tall.

I am also thankful to the senior and junior colleagues in our laboratory, whose camaraderie and help in both academic and daily matters have made this journey warm and meaningful. I have been fortunate to walk this path among such fine individuals.

My heartfelt thanks go to JAIST for providing an inspiring and inclusive research environment. The freedom to explore and the resources available here have enabled me to focus on my work and develop my ideas to the fullest.

And last but not least, I would like to thank my dear girlfriend, Jiali, for the understanding, joy, and encouragement. In both the calm and turbulent moments, your companionship has been a source of light and strength.

Thank you all for being part of this journey.

Table of Contents

List of physical parameters

Re	Reynolds number
Ca	Capillary number
Ma	Marangoni number
ρ	Density (kg/m^3)
v	Characteristic velocity (m/s), (mm/min), (μm/min)
μ	Viscosity (Pa·s)
D_H	Hydraulic diameter (m)
L	Characteristic length (m)
γ	Surface tension (N/m)
C_0	Initial concentration (wt%)
C_S	Saturated concentration (wt%)

Chapter 1

General Introduction

1.1 Dissipative structure and pattern formation

The natural world abounds with patterns—ripples on sand dunes, stripes on zebras, convection rolls in heated fluids. While many such patterns may appear static or preordained, they often emerge spontaneously in systems driven far from thermodynamic equilibrium.[1] The formation of ordered structures in nonequilibrium systems is an important topic in modern science and engineering. Such structures emerge through the interaction of energy dissipation, transport processes, and self-organizing mechanisms, as explained by Ilya Prigogine's theory of dissipative structures.[2,3] This groundbreaking insight was that entropy production does not always lead to disorder; instead, it can catalyze the formation of coherent, dynamic structures when nonlinear interactions and instabilities are present. This principle is widely applicable to pattern formation processes in a variety of fields ranging from biological morphogenesis to nanomaterial preparation.

In open systems far from equilibrium, dissipative structures will spontaneously develop spatial or temporal patterns during continuous energy input and dissipation. One of the earliest and most well-known examples is Rayleigh-Bénard convection (**Figure 1.1a**),[4] which was observed in the early 20th century. A fluid heated from below and cooled from above spontaneously develops a regular array of convection rolls beyond a critical temperature gradient. Independent of the scale, convection reveals magnificent patterns in nature, such as the Salt polygons (**Figure 1.1b**).[5] Spatiotemporal patterns in nonequilibrium also could be find in chemical systems. Belousov-Zhabotinsky (BZ) reaction,[6] which was proposed in 1951, a non-equilibrium chemical oscillator that produces concentric rings, spirals, and other striking spatial patterns (**Figure 1.1c**). Based on the spatial-temporal rhythms of such oscillations, Yoshida R. et al. have developed self-oscillating gels from peristaltic motion actuator gel into periodical beats-like gel as human heart. [7] Chemical spatiotemporal patterns in open systems also play an important role in life systems, such as the Tricarboxylic Acid (TCA) cycle (**Figure 1.1d**).[8] More broadly and in a more complex sense, a reaction-diffusion system could spontaneously

generate spatial patterns if certain conditions are met. The turing patterns (**Figure 1.1e**),[9] first proposed by Alan Turing in 1952, demonstrate the role of differential diffusion rates and appropriate nonlinear feedback. This theoretical result laid the groundwork for understanding how simple chemical or biological interactions could give rise to complex morphologies, as seen in animal coat patterns, morphogenesis, and ecological spatial distributions (**Figure 1.1f**).[9] These nonequilibrium pattern-forming processes, ubiquitous in both natural and artificial systems, not only offer a scientific basis for aesthetics and artistic expression, but also provide profound insights into self-organization in nature and the fundamental dynamics of complex systems.

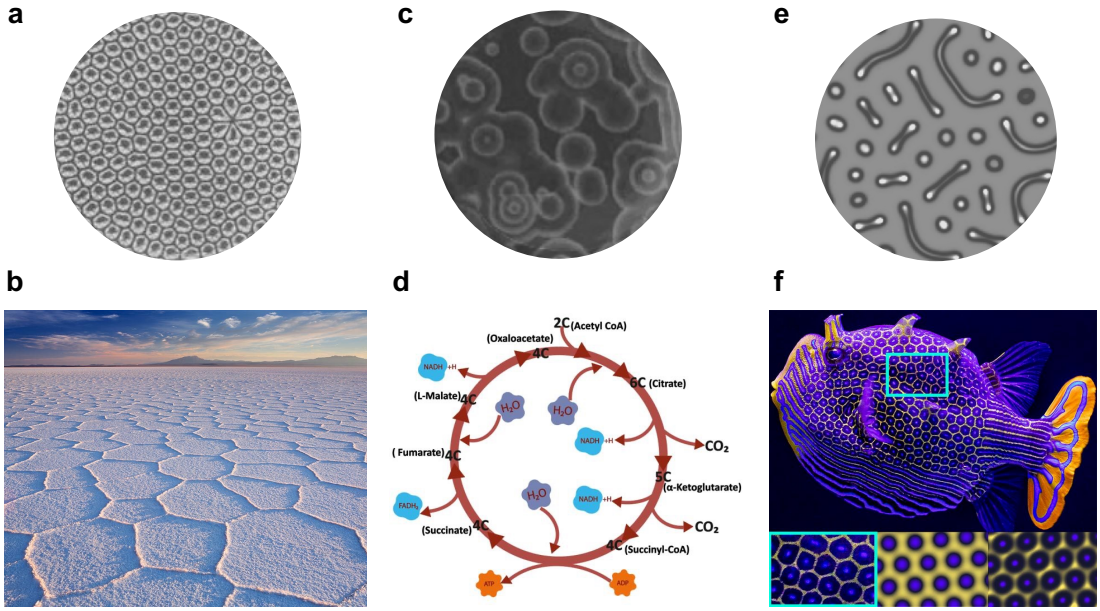

Figure 1.1 Dissipative structures and the formation of the typical patterns. a) Rayleigh–Bénard convection. [4] **b)** the salt polygons "Salar de Uyuni" in Bolivia.[5] **c)** Belousov-Zhabotinsky (BZ) reaction pattern.[6] **d)** The tricarboxylic acid cycle in mitochondria.[7] **e)** Turing pattern. **f)** Development of Turing patterns in an ornate boxfish.[9]

In dissipative structures, viscous fingering is a hallmark of nonequilibrium interfacial dynamics, traditionally observed when a less viscous fluid displaces a more viscous one within a confined geometry, such as in the classic Saffman–Taylor instability (**Figure 1.2a**).[10] Beyond this, fingering instabilities can also emerge spontaneously in

systems driven by thermal gradients (**Figure 1.2b**).[11] For instance, under imposed temperature gradients, interfacial instabilities arise between immiscible fluids like gas and silicone oil, leading to spontaneous viscous fingering without external mechanical forcing. Moreover, the viscous finger has been further extended to the evaporation of viscous dispersions. Under thermal energy input, the meniscus of air-liquid interface can undergo a dynamic "splitting" process, generating finger-like patterns due to local concentration gradients and surface tension instabilities and fixed as deposited patterns (**Figure 1.2c**).[12] These diverse manifestations of viscous fingering under thermodynamic nonequilibrium conditions highlight the intricate coupling between thermal, compositional, and hydrodynamic fields. Understanding these processes is not only fundamental to fluid physics, but also critical for advancing technologies in microfluidics, materials processing, and energy systems. More broadly, exploring pattern formation under nonequilibrium conditions continues to offer profound insights into self-organization, nonlinear dynamics, and the emergence of order in complex systems.

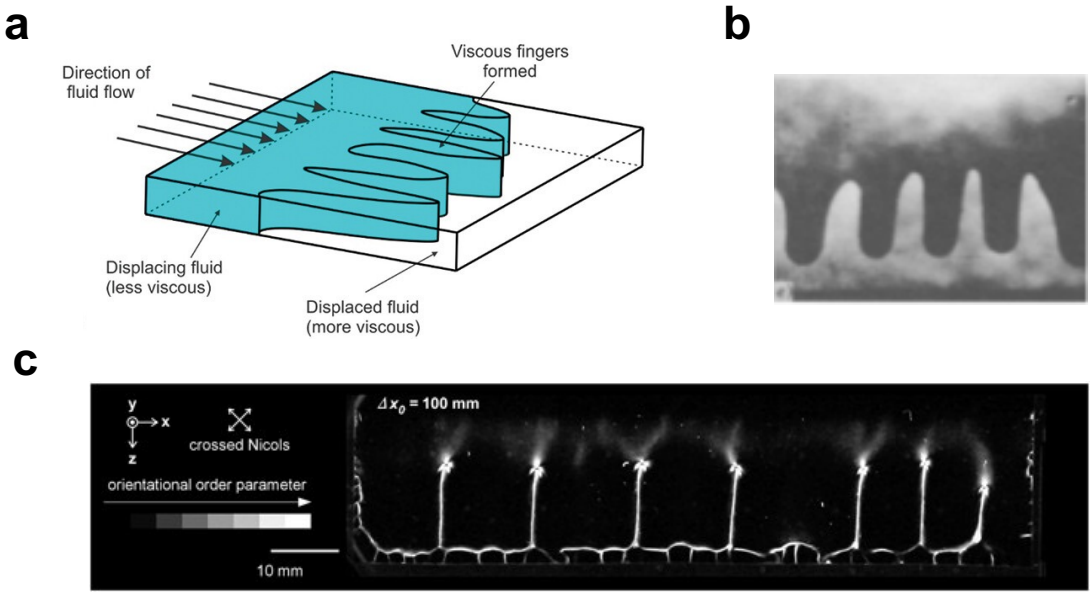

Figure 1.2 a) Viscous instability that occurs when a less viscous fluid displaces a more viscous fluid.[10] **b)** Spontaneous formation of exponential growth fingering pattern in viscous fluids under thermal gradient.[11] **c)** Meniscus splitting in limited space with

100 mm width, exhibited similar deposition intervals.[12]

1.2 Fluid dynamics in evaporation and deposition

As a typical example of a dissipative structure, Evaporation-Induced Self-Assembly (EISA) is a delicate process whereby the evaporation of a solvent drives the spontaneous organization of colloidal particles or molecules to form highly ordered structures. By continuous energy input via solvent evaporation drives the system far from equilibrium, giving rise to complex interplays among fluid flow, mass transport, and interfacial forces that produce a rich variety of deposition patterns. These patterns not only reveal the underlying physics of coupled transport processes but also hold significant technological promise in applications such as inkjet printing, microfluidic biosensing, and precision thin-film fabrication.[13,14]

A well-known case is the coffee ring effect, where asymmetric evaporation rates at the droplet edge induce capillary flows that transport suspended particles outward, resulting in ring-like stains (**Figure 1.3a**).[15-17] In contrast, under altered thermal or compositional conditions, interfacial stresses can trigger Marangoni flows that reorganize the internal circulation, suppress the ring, and yield uniform deposition. [18] These transitions are not random—they reflect shifts in the governing force balances, which are effectively captured by dimensionless numbers such as the Marangoni number (interfacial stress vs. viscous dissipation), the Capillary number (viscous vs. surface tension forces), and the Reynolds number (inertia force vs. viscous force). Their values provide a compact, scale-independent way to predict qualitative changes in flow behavior and pattern outcomes.

Beyond evaporating droplets, meniscus-guided coating (MGC) leverages the motion of a confined liquid meniscus to direct material assembly.[19] Despite its different geometry, MGC is governed by the same core competition among viscous, inertial, and surface-tension forces. By tuning parameters such as coating speed, substrate wettability, and thermal gradients, one can switch between uniform films and periodic patterns

(**Figure 1.3b**).[20] As in droplet systems, nondimensional analysis delineates the boundaries of different flow and deposition regimes, enabling predictive control over film morphology and performance. Adjusting coating speed, substrate properties, or thermal gradients shifts the flow regime, often leading to instabilities or changes in deposition morphology [21]. As in droplet systems, dimensionless analysis allows researchers to identify regime boundaries, optimize process conditions, and design for uniform or patterned films. [22]

Building on this perspective, the present study focuses on another interfacial deposition phenomenon, meniscus splitting, which occurs when an interfacial meniscus undergoes spontaneous splitting into multiple interfaces during fluid motion. This behavior, though less studied, presents a rich case of symmetry breaking and flow structure coupling in a finite geometry. [23,24] By applying the same hydrodynamic principles and scaling tools, we aim to interpret the onset and evolution of meniscus splitting through the lens of dimensionless parameters, providing a unified framework to link it with broader evaporation-induced deposition phenomena. Understanding such transitions is not only of theoretical interest in nonequilibrium systems but also holds practical relevance in microfluidics, precision coating, and capillary-driven assembly. Through this work, we seek to extend the use of fluid dynamic descriptors to a less-explored interfacial behavior, offering both mechanistic insight and predictive capability.

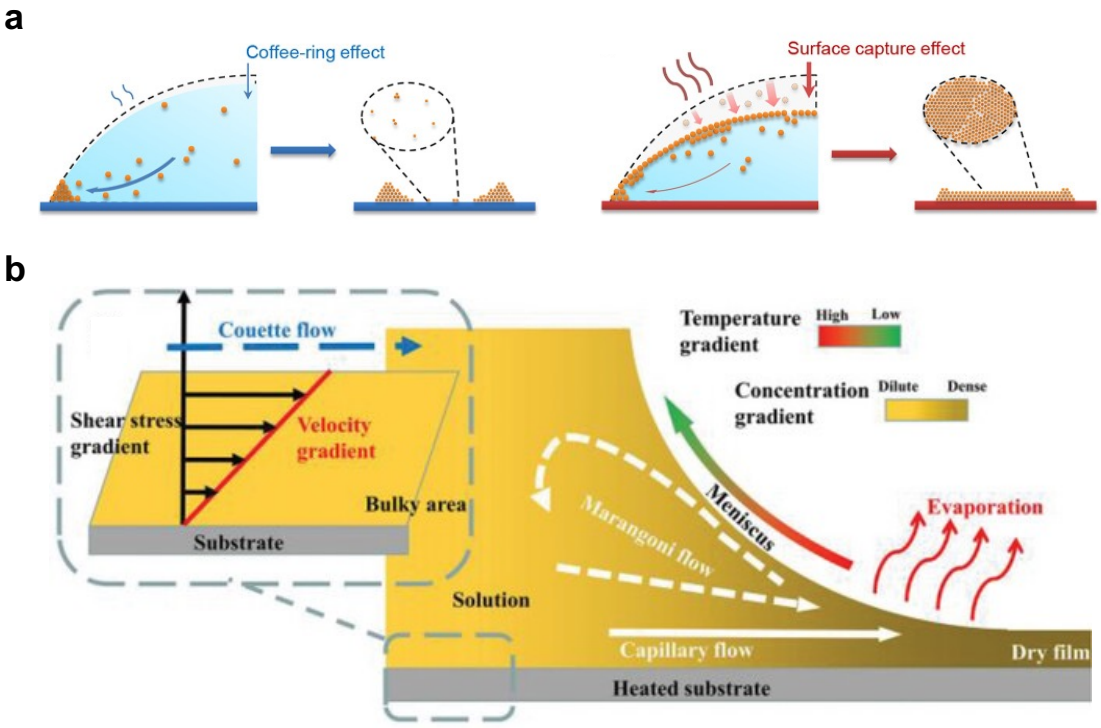

Figure 1.3 a) The schematic diagram of coffee ring pattern deposition and the uniform pattern deposition. **b)** Schematic diagram of internal flow of meniscus. The white dotted arrow indicates the direction of the Marangoni flow, and the solid arrow indicates the direction of the capillary flow.[16]

1.3 Meniscus splitting phenomenon during evaporation

Owing to viscous dissipation, viscous fluids between parallel plates will form a typical fingering pattern under a thermodynamic gradient.[11] Such viscous fingering exists temporarily in the fluid and would disappear when the system reached thermodynamic equilibrium. Based on viscous fingering,[25] meniscus splitting phenomenon was observed in the Hele Shaw cell with ~ 1 mm gap during the evaporation of polysaccharide dispersions. Under continuous thermal energy input, the polysaccharides undergo flocculation at the air–liquid interface and subsequently deposit as nucleation, which spontaneously divide the original meniscus into multiple smaller menisci. As a characteristic pattern, vertical membranes are forming by the evaporation, as shown in **Figure 1.4a** and **1.4b**, called meniscus splitting.[26] This process is exemplified by aqueous polysaccharide mixtures (*e.g.*, sacran, $M_w > 10^7$ g/mol), while the deposited polymers bridge the millimeter-scale gap in the Hele-Shaw cell via capillary-driven polymer deposition. This strategy successfully fixed the periodic finger patterns from viscous fluids into the deposited polymers, while deposition pattern exhibits spatial periodicity.[27] The meniscus splitting phenomenon is not only observed in the self-assembly of sacran dispersion, but also demonstrated in the drying of other aqueous polysaccharides dispersion, such as pectin, xanthan gum, and chitosan.[28-30] Thus, the meniscus splitting phenomenon is expected to involve physical rules related to temporal evolution, especially the nonequilibrium period prior to nucleation. This splitting pattern, observed under nonequilibrium conditions, may shed light on the underlying mechanisms and offer insights into the formation of geometric patterns.

Beyond the phenomenon, not limited to the millimeter-scale evaporation process, the ordering deposition pattern is manifested to the deposited vertical membranes, which exhibit oriented microstructures.[31,32] Such orientational structures within the polysaccharide membranes endow them with unique swelling behaviors based on the original characteristics, such as uniaxially swelling of xanthan gum membrane [33], cation-

responsive anisotropic swelling of pectin membrane [34], and reversible pH-responsive chitosan membrane [30]. Therefore, such evaporation strategy shows great potential for controlling polymer deposition patterns, paving the way for novel strategies in soft material design. Also, these facts enhanced the importance of elucidating the deposition mechanism underlying the meniscus splitting phenomenon.

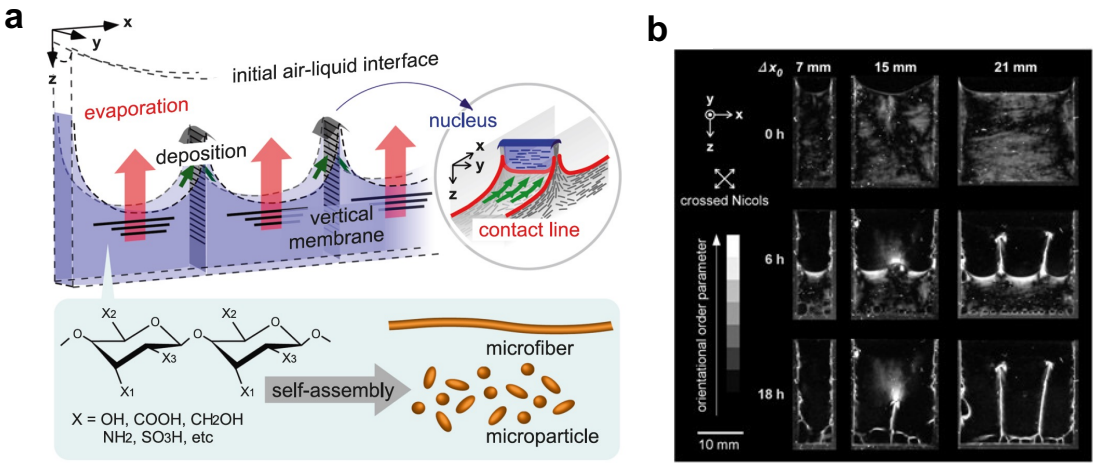

Figure 1.4 Meniscus splitting with multiple nuclei deposition to form vertical membrane walls.[26] **a)**. Schematic diagram of polysaccharide particles assembly during evaporation in meniscus splitting. **b)** Time courses of vertical membrane formation during drying from Hele–Shaw cells with a given X-width.

1.4 General purpose

In this work, to understand the meniscus splitting phenomenon that occurs in viscous polysaccharide dispersions during evaporation accompanied by thermal energy input only. We firstly aim to investigate the interfacial behavior, especially the interfacial fluctuation. We explored the underlying hydrodynamic principles and mechanisms in the unique evaporation phenomenon. Based on the important role of viscous and inertial forces in the evaporation process, we emphasize the characteristics Reynolds number of the meniscus splitting phenomenon.

Secondly, we found that the emergence of internal Marangoni circulation during the nonequilibrium process. By analyzing the velocity distribution in the liquid phase during evaporation, we demonstrate the importance of circulation confluence and the formation of the skin layer while nucleation.

Moreover, based on the synchronous and asynchronous nucleation, we demonstrate the important role of plumes during Marangoni convection in asynchronous nucleation by control the geometry of the Hele Shaw cell. However, in another polysaccharide dispersion system (Xanthan gum dispersion), which exhibited nucleation in meniscus splitting, there is no convection pattern, and it showed synchronous nucleation.

References

[1] Goldbeter, A. *Philos. Trans. R. Soc. A.* **376**, 20170376 (2018).

[2] Prigogine, I., & Nicolis, G. *J. Chem. Phys.*, **46**, 3542 (1967).

[3] Prigogine, I. *Science*, **201**, 777 (1978).

[4] Bergé, P., & Dubois, M. *Contemp. Phys.,* **25**, 535 (1984).

[5] Lasser, J., Nield, J. M., Ernst, M., Karius, V., Wiggs, G. F., Threadgold, M. R., ... & Goehring, L. (2023). Salt polygons and porous media convection. Physical Review X, 13(1), 011025.

[6] Zhabotinsky, A. M. Belousov-zhabotinsky reaction. *Scholarpedia*, **2**, 1435 (2007).

[7] Lee, W. S., Enomoto, T., Mizutani Akimoto, A., & Yoshida, R. *Chem. Mater.*, **36**, 2007 (2024).

[8] Antoniewicz, M. R. Methods and advances in metabolic flux analysis: a mini-review. *J. Ind. Microbiol. Biotechnol.*, **42**, 317-325 (2015).

[9] Alessio, B. M., & Gupta, A. Diffusiophoresis-enhanced Turing patterns. *Sci. Adv.*, 9 (2023).

[10] Cvetkovic, I., & Milicev, S. *Adv Phys X.*, **9** (2024).

[11] J. B. Brzoska, F. Brochard-Wyart, F. Rondelez, *Euro phys. Lett.*, **19**, 97 (1992).

[12] Kondepudi, D. K., De Bari, B., & Dixon, J. A. *Entropy*, **22**, 1305 (2020).

[13] Lin, Z. (Ed.). Evaporative self-assembly of ordered complex structures. World Scientific (2012).

[14] Li, W., Zhang, C., & Wang, Y. *Adv. Colloid Interface Sci.*, 103286 (2024).

[15] Han, W., & Lin, Z. *Angew. Chem., Int. Ed.*, **51**, 1534 (2012).

[16] Li, Y. F., Sheng, Y. J., & Tsao, H. K. *Langmuir*, **29**, 7802 (2013).

[17] Li, Y., Yang, Q., Li, M., & Song, Y. *Sci. rep.*, **6**, 24628 (2016).

[18] Hu, H., & Larson, R. G. *J. Phys. Chem. B.*, **110**, 7090 (2006).

[19] Gu, X., Shaw, L., Gu, K., Toney, M. F., & Bao, Z. *Nat. commun.*, **9**, 534 (2018).

[20] Ren, C., Cao, L., & Wu, T. *Small*, **19**, 2300151 (2023).

[21] Lade, R. Flow and Drying Dynamics in Gravity-and Capillary-Driven Coating Processes (2017).

[22] Ajaev, V. S., Gatapova, E. Y., & Kabov, O. A. *Adv. Colloid Interface Sci.*, **228**, 92 (2016).

[23] Crawford, J. D., & Knobloch, E. *Annu. Rev. Fluid Mech.*, **23**, 341 (1991).

[24] Grotberg, J. B., & Jensen, O. E. *Annu. Rev. Fluid Mech.*, **36**, 121 (2004).

[25] Maher, J. V. *PRL*, **54**, 1498 (1985).

[26] K. Okeyoshi, M. K. Okajima, T. Kaneko, *Sci. Rep.*, **7**, 5615 (2017).

[27] K. Okeyoshi, *Polym. J.*, **52**, 1185 (2020).

[28] K. Okeyoshi, M. Yamashita, K. Budpud, G. Joshi, T. Kaneko, *Sci. Rep.*, **11**, 767 (2021).
[29] L. Wu, I. Saito, K. Hongo, K. Okeyoshi, *Adv. Mater. Interfaces*, **10**, 2300510 (2023).
[30] T. K. L. Nguyen, Y. Tonomura, N. Ito, A. Yamaji, G. Matsuba, M. Hara, Y. Ikemoto, K. Okeyoshi, et al. *Langmuir*, **40**, 11927 (2024).
[31] Budpud, K., Okeyoshi, K., Okajima, M. K., & Kaneko, T. *Small*, **16**, 2001993 (2020).
[32] Okajima, M. K., Mishima, R., Amornwachirabodee, K., Mitsumata, T., Okeyoshi, K., & Kaneko, T. *RSC Adv.*, **5**, 86723 (2015).
[33] Joshi, G., Okeyoshi, K., Mitsumata, T., & Kaneko, T. *J. Colloid Interface Sci*., **546**, 184 (2019).
[34] I. Saito, L. Wu, M. Hara, Y. Ikemoto, T. Kaneko, K. Okeyoshi, et al. *ACS Appl. Polym. Mater.*, **4**, 7054 (2022).

Chapter 2

Interfacial fluctuation during meniscus splitting

2.1 Introduction

Dissipative structures have been historically researched in numerous fields using soft materials. [1] In the development of phenomena of viscous fingering driven by thermal gradients, [2,3] we successfully obtained millimeter-scale patterns by drying some aqueous polysaccharide dispersions, such as pectin, xanthan gum, and sacran. [4,5] Spatial patterns are formed by the splitting of the meniscus with ordered depositions of self-assembled polysaccharides (from one space into multiple spaces) (**Figure 2.1**).We controlled the macroscopic interface motion in one direction and successfully fixed the spatial patterns from the aqueous fluids to reassemble the polymer based on water evaporation in contrast to conventional fingering patterns transiently showing spatial patterns and their disappearance due to the instabilities. [6-10] There are optimum ranges for controllable parameters in meniscus splitting, such as the initial polymer concentration, drying temperature, cell geometries, and types of polymers with specific characteristics, like viscosity. [11,12] As a result of interface fluctuations, the interface contact line induces the polymeric orientation and layered structures in the submicron scale using capillary forces.[5] During the period in which an initial interface transforms into multiple interfaces, there exist obvious fluctuations, however, it is still uncertain how the second nucleus will form.

In this chapter, we reported on interfacial fluctuations following the splitting of the meniscus into three menisci to expose the aspects of the dissipative structure. In contrast to the splitting of the meniscus into two parts, the interface becomes more unstable when three menisci are formed, and a larger degree of freedom is provided for the two nuclear positions. When evaporation conditions, such as the cell width, are fixed, the number of split menisci is determined with high probability (see Figure 2.1). The first nucleus is deposited to split the distance of the cell width equally rather than on the center of the width. For example, when the cell width is ~ 25 mm, and one initial evaporative interface changes into a wavy shape and splits into three menisci. The interface never changes

shape to form the first nucleus around the center of the width nor does it ever split into four. Before deposition nucleation, the interface with a precursor makes three concave menisci, that is, the interface recognizes the finite space. During water evaporation, the polymeric precursor accumulates on the interface in a nonequilibrium environment, that is, drying and wetting. This situation induces a wavy fluctuation which exhibits the recognition of spatial finiteness. Considering this process, the interfacial behavior of meniscus splitting should include physical rules based on temporal evolution.

The drying process was performed in a box and monitored in controlled temperature and humidity conditions. The phenomena were statistically examined and spatiotemporally analyzed by deriving the evaporation velocity at characteristic positions. *Re* was evaluated to understand the effects of physical parameters on the splitting. Life in low-Re cases ($Re < \sim 10^{-4}$) exhibits attractive mass-transportation or swimming motions in microorganisms using flagella or cilia.[13] In the realm of material design, laminar flow at low Reynolds numbers enables molecules to exhibit their flexibility, leading to the creation of distinct microstructures tailored for specific materials.[14] These examples in actual, viscous underwater environments show that huge potentials exist at low Re, regardless of the size or scale. While surface tension plays a crucial role in the interfacial fluctuation generation during meniscus splitting, quantitative analysis from surface tension remains challenging due to the rheological properties of high-concentration polymer dispersion. Thus, the in vitro meniscus-splitting phenomena were examined from a hydrodynamic perspective instead of a mechanical perspective.

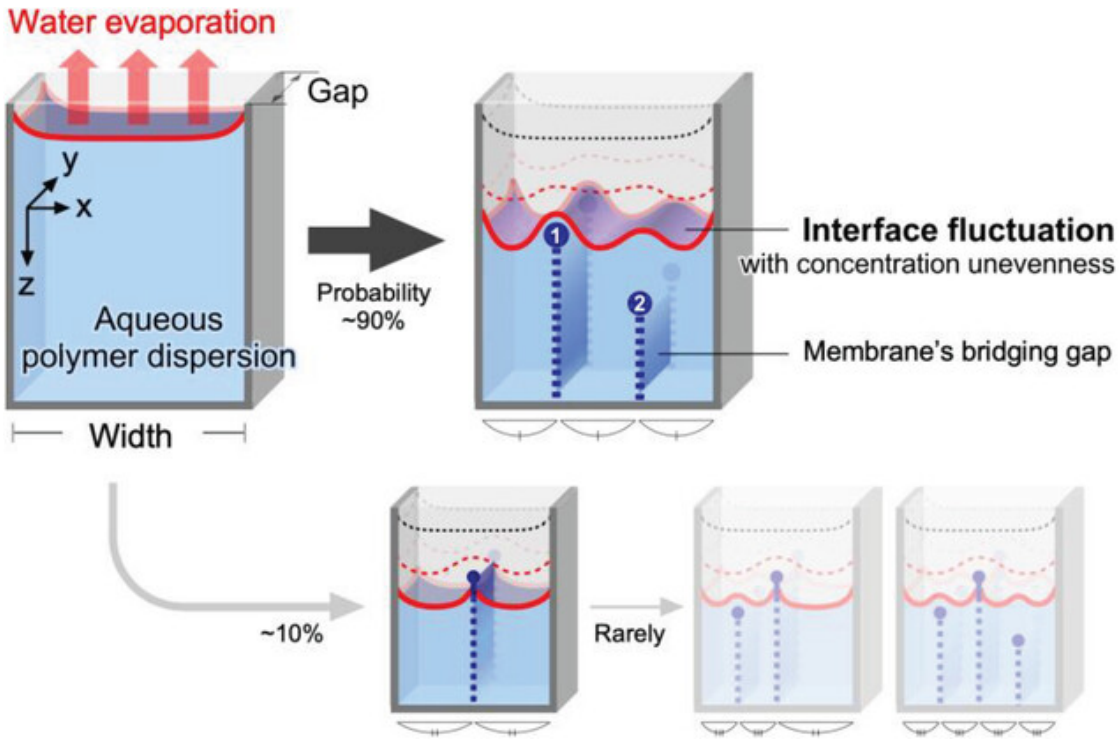

Figure 2.1 Schematics of meniscus splitting into three parts owing to interface fluctuation and recognition of spatial finiteness. When the conditions (including the cell width) are fixed, one meniscus splits into three parts (but rarely into two) with nucleation at the center of the cell width (following a split into three or four menisci).

2.2 Experimental

2.2.1 Materials

Citrus pectin with a molecular weight in the range of 20–400 kDa was purchased from Nacalai Tesque, Japan. As a low-methoxy pectin, it contains more than 50% galacturonic acid units and 11% methoxy groups. The pectin powder was dispersed in pure water at room temperature, and the small number of impurities and air bubbles were removed by brief centrifugation (6000 rpm, 3 min). The supernatant dispersion was used for sample preparation. The aqueous pectin dispersion was kept in a refrigerator and used within a week to avoid changes in properties. The Hele Shaw cell for evaporation is made by two glass substrates and a "U" shape PVC sheet (**Figure 2.2a**). The glass substrates were purchased from Matsunami Glass Ind. Ltd., Japan.

2.2.2 Drying experiment for spatiotemporal analysis

The pectin dispersion was injected into the Hele Shaw cell and placed in a ≈1 L observation box with controlled temperature and humidity through a temperature-controlled air circulation pump (**Figure 2.2b**).[15] The internal space temperature of the box was controlled by using two ways. One was connecting a heat pen with a circulating tube and another one was rubber heaters attached on the inner walls of the box. The relative humidity in the box was controlled by keeping the temperature constant and flowing air circulation. The correlation of the temperature and the relative humidity was checked as shown in **Figure 2.2c**, and it could be confirmed that it was possible to control the humidity constant during the drying experiments. During the drying process, the samples were monitored through glass windows, and images were captured at certain time intervals (10 min). The interfacial positions (X, Z) were determined by setting the cell's top corner as the coordinate origin (O). To obtain the Z-positions from the images in a time course, the image sequences at each X-position were prepared using the software package ImageJ (National Institutes of Health, Bethesda, MD, USA) and analyzed by Multikymograph. The Z-positions in the time course were plotted using GetData Graph

Digitizer through grayscale recognize (**Figure 2.2d**). The interfacial velocity(d*Z*/d*t*) was estimated using the plots (*t*, *Z*).

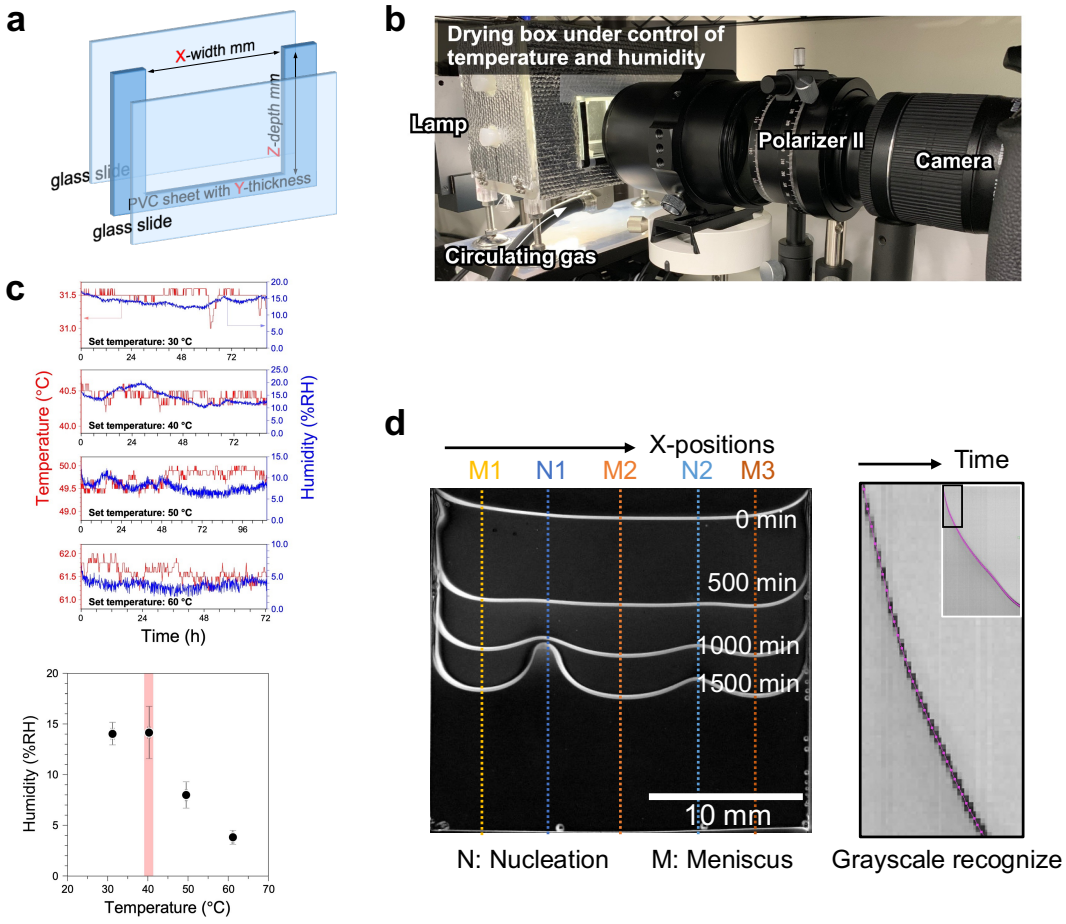

Figure 2.2 Experimental setup used for spatiotemporal analysis of evaporation process. a) The Hele Shaw cell is made by two glass substrates and a PVC sheet with given shape. The size of the cell is *X*-width, *Y*-gap, *Z*-depth. **b)** The snapshot of the observation box. **c)** Time course of the actual temperature and relative humidity (RH) in the observation box at a given set temperature, and the correlation of temperature with RH in the observation box. By measuring the time course of the actual temperature and humidity in the drying box, the RH at 40 °C was estimated to be 14.2 ± 2.5% RH. **d)** Spatiotemporal analysis of evaporation process, "N" means the given positions of Nucleation, "M" means the given positions of meniscus. The right figure is an example of time course curve at a meniscus position. *The data **c** was obtained by other members.

2.2.3 Characterization of aqueous polymer dispersions

The absolute viscosities of aqueous polymer dispersions were measured using an electro magnetically spinning viscometer (EMS-1000S, Kyoto Electronics Manufacturing Co., Ltd.) in temperature-controlled and inhibition of water evaporation conditions. Measurement conditions were as follows: Probe: Ti-5.0 mm, probe rotation speed: 1000 revolutions per minute, maintenance time: 600 s, repeat times: 10, measurement interval: 10 s, measurement times corresponding to different viscosities in the range of 0.5–45 min. The density of the sample was measured using a benchtop density meter (DMA4501, Anton Paar). The characterization was performed at specific constant temperatures. The size of pectin particles was confirmed by optical microscopic image of the deposited particles on glass substrates (**Figure 2.3a** and **b**) and the Z-average diameter by dynamic light scattering (Malvern Panalytical Ltd.) with 0.01 wt% concentration pectin dispersion (**Figure 2.3c**).

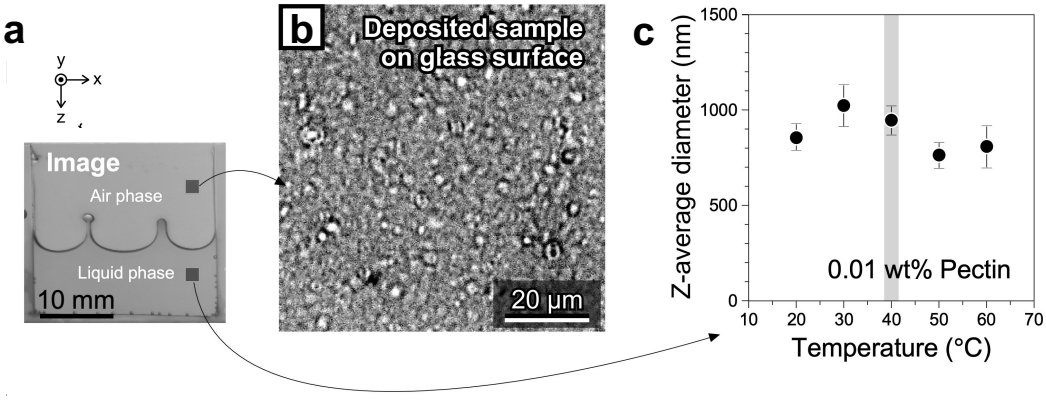

Figure 2.3 a) Snapshot of the meniscus splitting process. Particle size was confirmed by the deposited pectin on the glass substrate and the pectin particles in the dispersion. **b)** Optical microscopic image of pectin particles deposited on the glass surface. **c)** Z-average diameter of pectin in an aqueous dispersion measured by Dynamic Light Scattering with 0.01 wt% pectin dispersion at given temperatures.

2.3 Results and discussion

2.3.1 Statistical analysis of nucleation positions

Figure 2.4a show the time course of the evaporative interface and the deposition nucleation from the aqueous pectin dispersion in cells with 1 mm gaps and 5, 15, and 25 mm widths at 40 °C. As the water evaporated, under the dominance of capillary forces in Y-direction, the local polymer concentration on the interface increased drastically to deposit pectin by bridging the 1 mm gap. During drying, the evaporative meniscus split into two parts from the 15-mm-width cell and into three parts from the 25 mm-width cells. The split interfaces induced a continuous polymeric accumulation at specific positions by bridging the gap.[5] Moreover, the number of nuclei and the interval were strongly affected by the cell width. Based on the results, the interval in the width direction was less than 10 mm with a high probability. This is likely because there exists a state of quasi-equilibrium between the air pressure and liquid pressure, like the stable semi-ellipse that formed when an air bubble was squashed in a 1 mm gap.[16,17] The reproducibility of the number of nuclei was evaluated with 20 trials in each condition at 40, 50, and 60 °C (**Figure 2.4b**). At any drying temperature, the 15-mm-width cell induced the generation of one nucleus with a probability of 100%, and the 25-mm-width cell induced the generation of two nuclei with a probability > 80%. Thus, multiple nucleations occur because the split meniscus has the advantage of increasing the area of the evaporative interface with polymer depositions at specific positions.

To validate the specific depositions in detail, the positional information of the nucleus was collected. **Figure 2.4c** shows the distribution of the nuclear position (X_N, Z_N) in cells with widths equal to 15 and 25 mm. The positions in the cell with a 15 mm width were estimated to be (7.5 ± 0.1, 9.9 ± 0.4), (7.3 ± 0.1, 10.5 ± 0.2), and (7.6 ± 0.2, 15.0 ± 0.7) at 40, 50, and 60 °C, respectively, whereas X_N was mostly around the center at any drying temperature, and Z_N became deeper as the temperature increased. This is because the viscosity of the dispersion became lower at higher temperatures. As in the case of the

25-mm-width cell, the distributions were normalized based on the following rule: the nucleus with a shallower Z_N was placed in a smaller X-position as the first nucleus. Herein, two clear distributions were observed in the X-direction; for example, at 40 °C, ($X_{N1,\ 40°C}$, $Z_{N1,\ 40°C}$) = (6.5 ± 0.3, 7.9 ± 0.5) and (X_{N2}, 40C, $Z_{N2,\ 40°C}$) = (15.9 ± 0.6, 11.2 ± 0.7). The two distributions result from the interfacial instability of the accumulated polymer and the critical wavy meniscus. At the meniscus with the concentrated polymeric layer, the mechanical stress would be loaded from both sidewalls. Even such a situation, the polymer particles are provided and accumulated from the liquid phase. To release the mechanical stress and keep water evaporation, the interface is deformed by making a wavy shape with multiple specific points for polymer deposition. This is similar to skin layer generation and pattern formation in the volume changes of polymer gels, which is described as mechanical instabilities.[18,19] Furthermore, the difference between Z_{N1} and Z_{N2} is due to the insufficient widening of the area of the evaporative interface by the first nucleus, which induces the second deposition nucleus to widen the area further. As the drying temperature increased, both Z_{N1} and Z_{N2} increased. This result supports the consideration of the 15-mm-width cell, which was affected by viscosity. Thus, this statistical analysis revealed that the X-width of the cell determines the number of nuclei in meniscus splitting and nuclear positions.

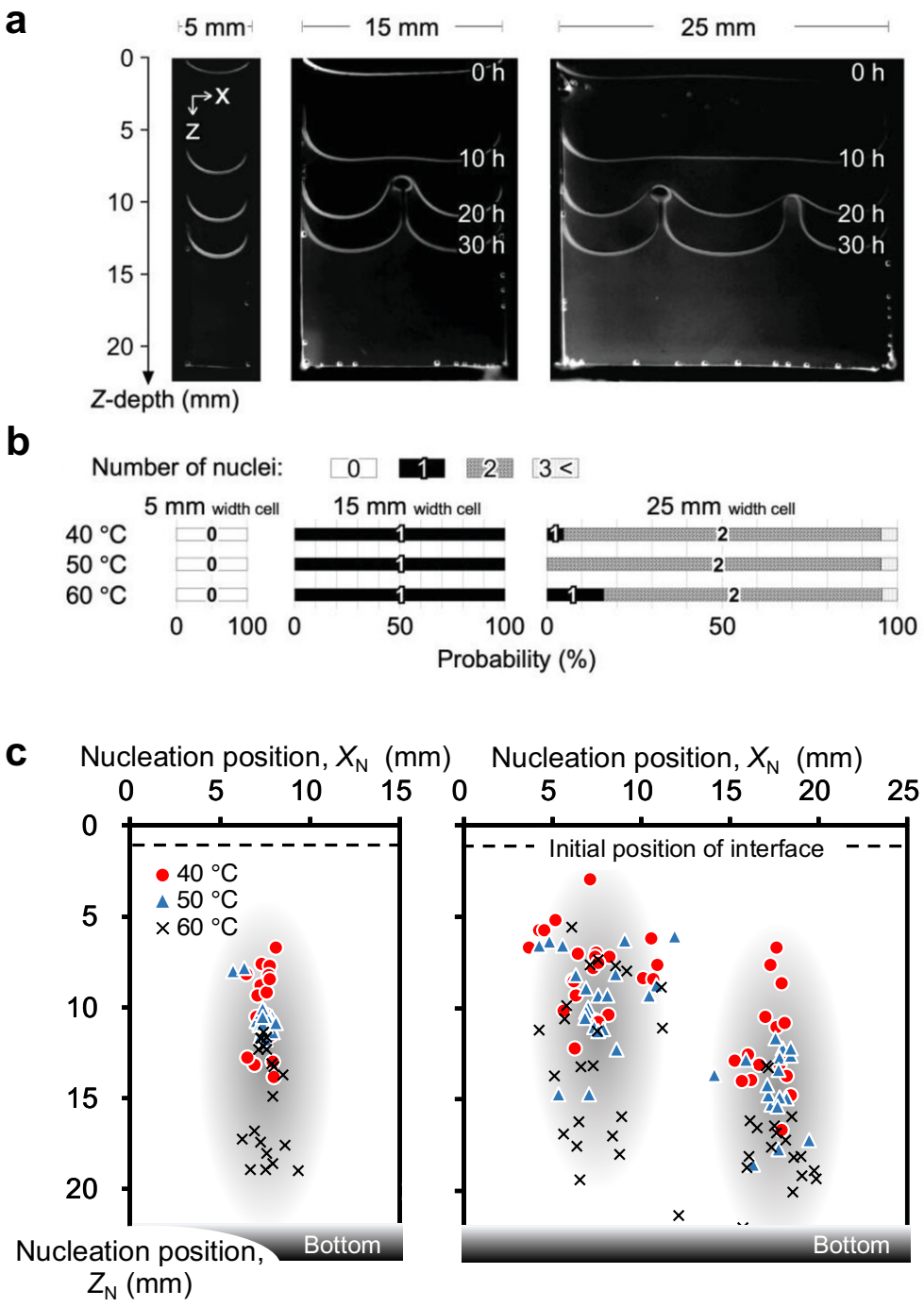

Figure 2.4 Recognition of spatial finiteness and the effect of cell width on the number of nuclei. a) Images of the drying process with meniscus splitting in given cells (X-width, 1 mm gap, 23 mm depth, drying temperature: 40 °C, and initial concentration of pectin, 6 wt%). **b)** Probability of the number of nuclei at a given temperature and cell width. Twenty trials were conducted at each condition. **c)** Statistical space distribution of the nuclear position (X_N, Z_N) from cells with 15 and 25 mm widths at a given temperature. (The data was obtained by other members). *The data was obtained by other members.

2.3.2 Spatiotemporal analysis of interfacial fluctuations

Focusing on the interfacial fluctuation and two nucleations, spatiotemporal changes were analyzed using a 6.0 wt% aqueous pectin dispersion in a cell (25 mm, 1 mm, ≈ 23 mm) that was used for drying at 40 °C. The interfacial Z-depth was monitored at the characteristic X-positions for meniscus growth (**Figure 2.5a**): M1, M2, and M3and nuclei growth (N1 and N2). **Figure 2.5b, c** shows the time course of the Z-depth (*Z*) the interfacial velocity as the interfacial position motion (d*Z*/d*t*), respectively. Figure 2.5b shows that the change in interfacial Z-depth of the pectin dispersion is slower than that of pure water. This is because then dispersed polymer inhibits water evaporation. This situation induces an unevenness in polymer concentration beneath the evaporative interface as a colloidal suspension.[20] In fact, the rates of the time courses at N1 and N2 gradually decrease and fix the Z-positions at time lags of 1200 and 1800 min, respectively. This is also confirmed by the time course changes of the velocity in Figure 2.5c. Comparing the snapshots visually helps us understand relative differences. To examine the time course changes before the visible nucleation (0–900 min), the differential in the Z-depth at each position was analyzed and plotted as d*Z*/d*t* in Figure 2.4c. In the time courses of 100–300 min, values of d*Z*/d*t* at N1, N2, and M2 (≈ 8.6 μm min^{-1} at 200 min) are smaller than those at M1 and M3 (≈ 10.4 μm min^{-1} at 200 min) near the side walls. This is because the two side walls provide larger evaporative interface near points of M1 and M3 than near point of M2. During the water evaporation, the M1 and M3 interface initially expand to counteract the inhibition of evaporation caused by the increase in the polymer concentration. These results for the induction time (0–300 min) mean that the interface fluctuation and nuclear X-positioning have already started. After ≈ 600 min, d*Z*/d*t* at M2 approached the same velocity as that at M1 and M2; d*Z*/d*t* did not synchronize and behaved as a monotonically decreasing function with respect to the induction time. This interface fluctuation was due to the inhomogeneous rearrangement of the accumulated polymer clusters in the X-direction.

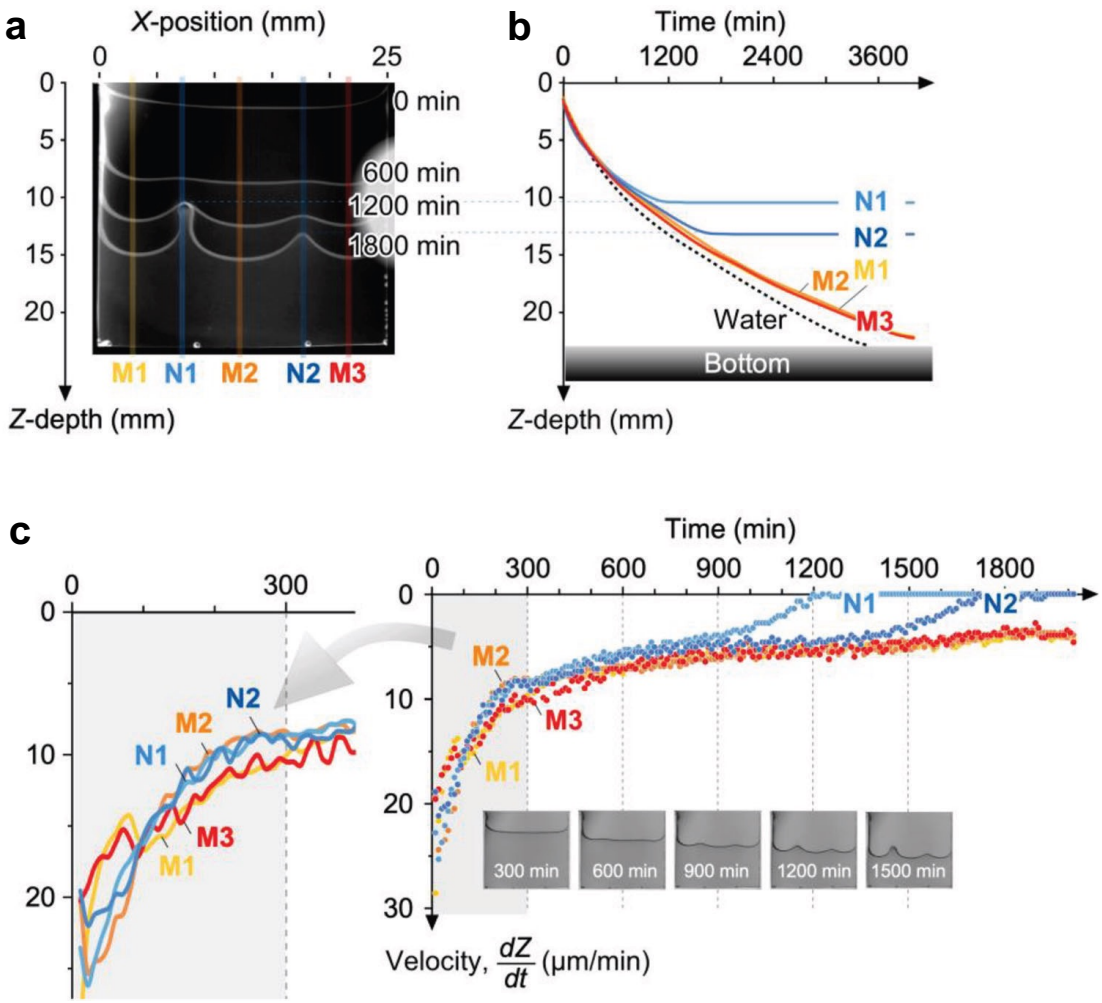

Figure 2.5 Spatiotemporal analysis of the meniscus splitting into three. a) Images of the drying process with meniscus splitting in a cell (25 mm width, 1 mm gap, 23 mm depth, initial concentration of pectin: 6 wt%, drying temperature: 40 °C). The lines represent characteristic X-positions: concave meniscus bottom parts (M1, M2, and M3), and nuclear top parts (N1 and N2). **b)** Time course curves of the interfacial Z-position at characteristic X-positions; that of pure water is also shown as a control. **c)** Evaporation velocity at characteristic X-positions and snapshots at different times.

2.3.3 Hydrodynamic evaluation of interfacial fluctuation and meniscus splitting

Considering our previous works, [5,21,22] the fluidic behaviors beneath the evaporative interface during the splitting process is critical for the formation of ordered polymeric micro-layered structures. Due to this precise arrangement of polymeric deposition, we focus on the correlation of fluid inertial force and the viscous force. By analyzing the temporal evolution of the interface as fluid flows downward, we verify the phenomena from a fluid dynamics perspective as a function of the dimensionless number *Re*, the ratio of the fluid inertial force to the viscous force was estimated as follows,

$$Re \equiv \frac{fluid\ inertial\ force}{fluid\ viscous\ force} = \frac{\rho u^2}{\mu\frac{u}{D_H}} = \frac{\rho u D_H}{\mu} \quad (1)$$

where ρ: density (kg·m^{-3}), u: interfacial velocity (m·s^{-1}), μ: dynamic viscosity (Pa·s), and D_H: hydraulic diameter (m). Because the accumulated state just before the polymer deposition is essential, the experimental parameters ρ and μ were evaluated as a function of polymer concentration *C* at constant temperatures (40, 50, and 60 °C); *u* was expressed as a function of time *t* using experimental data at characteristic X-positions (M1, M2, M3, N1, and N2). Since the evolution of the dispersion from the initial state to the split state in directly correlation with the X-width and Y-gap of the cell, we used the hydrodynamic diameter (D_H) of the Hele-Shaw cell as the geometry characteristic lengths, D_H was calculated as the rectangular duct, 4{(X-width) × (Y-gap)}/2{(X-width) + (Y-gap)}, 1.92 × 10^{-3} (m), when the cell size (X-width, Y-gap) was (25 mm, 1 mm). Parameters ρ and μ are described with approximate expressions $F(C)$ as shown in **Figure 2.6a** and **b**, and parameters *u* and D_H are expressed as time course change $F(t)$ as shown in **Figure 2.6c** and **d**. Changes in $F(C)$ owing to the extrapolation are used to predict the physical parameters at extremely high *C* values, but it is difficult to measure the local value precisely in experiments. Using these parameters and Equation (1), *Re* can be expressed as $F(C, t)$ for the viscous fluid. The Reynolds number within the interfacial layer serves to describe the motion state of individual positions at the interface. By comparing Reynolds numbers from characteristic regions, the interfacial behavior at a given time

could be reverted.

Figure 2.6e shows the estimation of the time course of *Re* by introducing fixed values of the concentration (6, 9, 12, 15, 18, and 21 wt%) into $F(C, t)$ to provide approximate guides of ΔRe at characteristic X-positions (N1, M2, and N2). Considering that the experimental limitation for dispersing pectin homogeneously in pure water seemed less than ≈ 12 wt%, the saturated polymer concentration (*C*s) should be close to this value. In a virtual experiment using the estimated Re, the drying starts from C_0 of 6 wt%, and *C* should increase constantly from $Re \sim 10^{-6}$. At ≈ 300 min, a critical inflection point was confirmed at all *X*-positions, and a plateau period was ensured in cases in which the concentration was fixed. This critical point was also confirmed in the analysis of the evaporation velocity, d*Z*/d*t* (see Figure 2.5c). After this timepoint, all the *Re* curves for N1, N2, and M2 exhibited distinct slopes. These results indicate that the induction time (0–300 min) should include the well-ordered process of creating concentration unevenness on the interface to form two nuclei. When *C* approaches *C*s (>12 wt%), the polymer deposits are attributed to the nuclei at positions N1 and N2 causing considerable ΔRe ($10^{-6} \rightarrow$ less than 10^{-8}). ΔRe in the laminar flow region should allow the well-ordered process from the sub-micrometer scale to form two nuclei in the millimeter scale.

Based on the spatiotemporal analysis and the validation of *Re*, the interface fluctuation is summarized as shown in **Figure 2.6f**. Considering that *Re* is the ratio of the fluid inertial and viscous forces, the temporal change in *Re* directly reflects a wavy fluctuation. When the water evaporation process begins, the polymer cluster accumulated on the interface and interfacial Z-depth simultaneously increases (state I). Initially, the interface near the two side walls increases as the boundary temporarily yields a larger change in the Z-depth to maintain the area for the water evaporation (state II). This process determines the shape of the interface fluctuation and the number of pre-nuclei. After the recognition of the space finiteness, definite splitting occurred to generate the first nucleus (N1), which was not generated from the center, and the interface predicted that the second one (N2) would be generated soon thereafter (state III). During state II,

the concentration unevenness on the evaporative interface was induced, and a gradual deposition was allowed at a specific position.

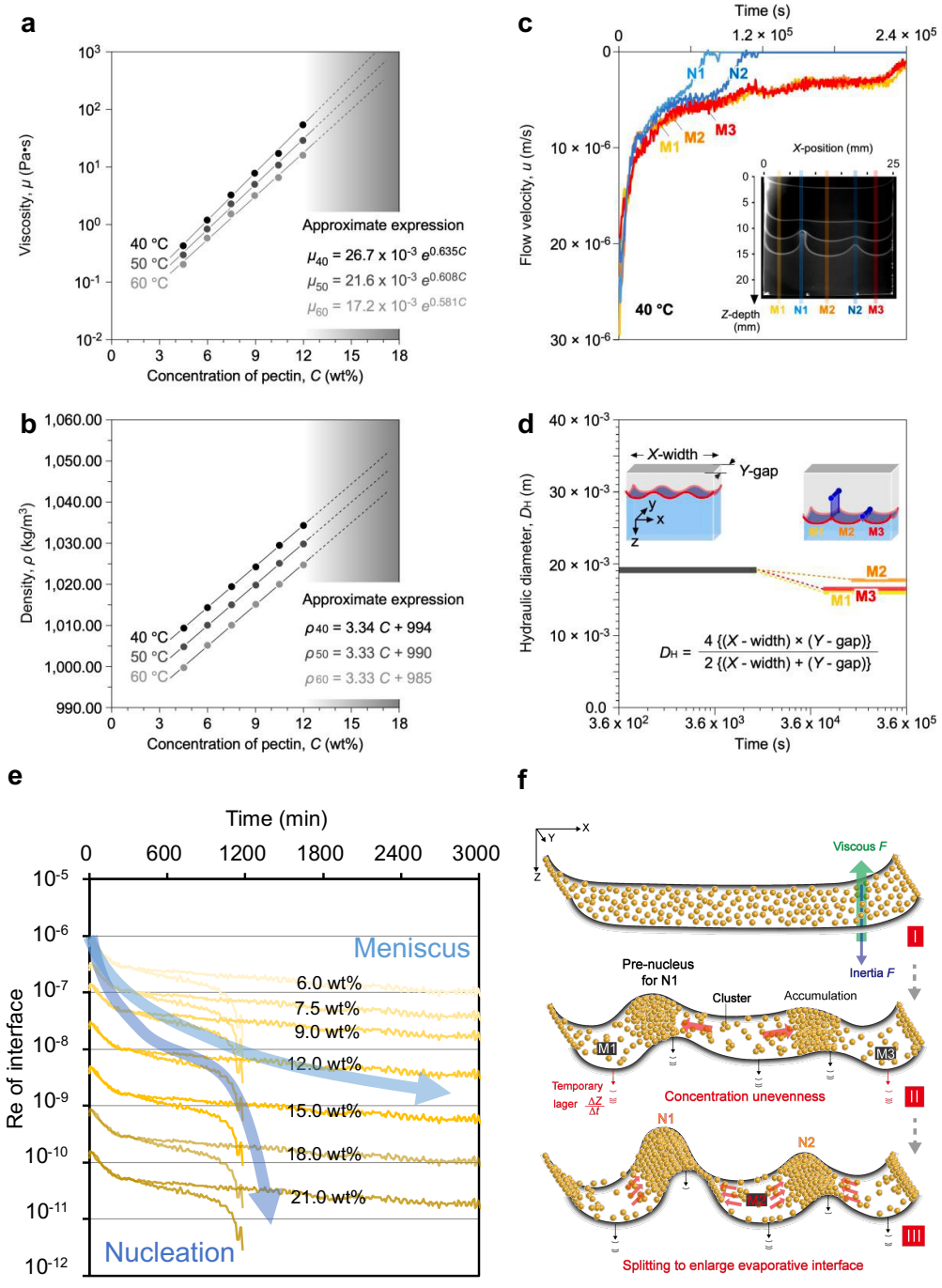

Figure 2.6 Spatiotemporal estimation of the Reynolds number during interfacial fluctuation. a) Viscosity μ of aqueous pectin dispersion as a function of pectin concentration and its approximate expression. **b)** Density ρ of aqueous pectin dispersion as a function of pectin concentration and its approximate expression. **c)**

Interfacial downward velocity u (dZ/dt) at characteristic positions (M1, M2, M3, N1, and N2). Cell (25 mm width, 1 mm gap, 23 mm depth), initial concentration of pectin: 6 wt%, and drying temperature: 40 °C. **d)** Estimation of hydraulic diameter as characteristic length D_H in a cuboid cell (25 mm width, 1mm gap, 23 mm depth). Herein, the extrapolations in the approximate curves (Fig. 2.5a and 2.5b) assume that the same correlations will exist at the higher concentration of 12 wt% (dotted lines) **e)** Estimation of the Reynolds number (Re) in a time course, calculated with actual μ, ρ, u, and D_H at given polymer concentrations. Arrows indicate the Re values at the X-positions (N1, N2, and M2). **f)** Hypothesis of the transition from accumulation to splitting to enlarge an evaporative interface based on three steps: I) induction period with polymeric accumulation on the evaporative interface; II) fluctuation period with a temporary acceleration on concave menisci sides; III) meniscus splitting into three parts with two asynchronous nucleations based on concentration unevenness.

2.3.4 Effect of hydraulic diameter in meniscus splitting

To close upon the concentration unevenness before the characteristic deposition, a comparison with some Y-gaps that are directly related to parameter D_H is discussed. When cells with 0.5 and 1.5 mm Y-gaps have the same parameter values, the polymer is deposited with different trends in each cell (**Figure 2.7a**). For the cell with a 0.5 mm Y-gap, the polymer is deposited horizontally at a smaller depth with lid- or T-shapes. Conversely, for the cell with a 1.5 mm Y-gap, the polymer is deposited at one or two specific points at a greater depth. These results can be expressed in the form of a correlation of D_H and Z_{N1} (**Figure 2.7b**). When the X-width was fixed at 25 mm, Z_{N1} was strongly affected by D_H and the shape. This result suggests that the Y-gap is an important factor in meniscus splitting. D_H shows a slight difference at an X-width > 15 mm. Consequently, as the X-width increases, the fluctuation can be developed into meniscus splitting with multiple nuclear formations. In fact, the evaporative meniscus is split into multiple menisci with similar Z_{N1} values in conditions of a fixed 1 mm Y-gap and X-widths >15 mm (**Figure 2.7c**). In our previous studies,[5,23] the effect of the cell width was also confirmed using the widths of 50 or 100 mm for other polysaccharides.

From these validations, the deposition trends can be explained by the initial unevenness on the evaporative interface. **Figure 2.7d** shows a schematic illustration of

the polymer clusters in the fluctuation to form pre-nuclei in the cases of the 25 mm width. From the cell with a 0.5 mm gap, the clusters easily bridge the gap at any X-position and make the evaporative meniscus larger near the sidewalls. By contrast, from the cell with a 1.5 mm gap, the clusters generate and retain multiple pre-nuclei because of the degree of freedom on the larger area of the interface. During water evaporation, these multiple pre-nuclei accumulate, and their numbers decrease to increase the area of the evaporative interface by forming multiple menisci. Thus, D_H critically affects the unevenness on the evaporative interface and number of specific depositions; for example, three splitting occur in the cell with a 1.0 mm gap.

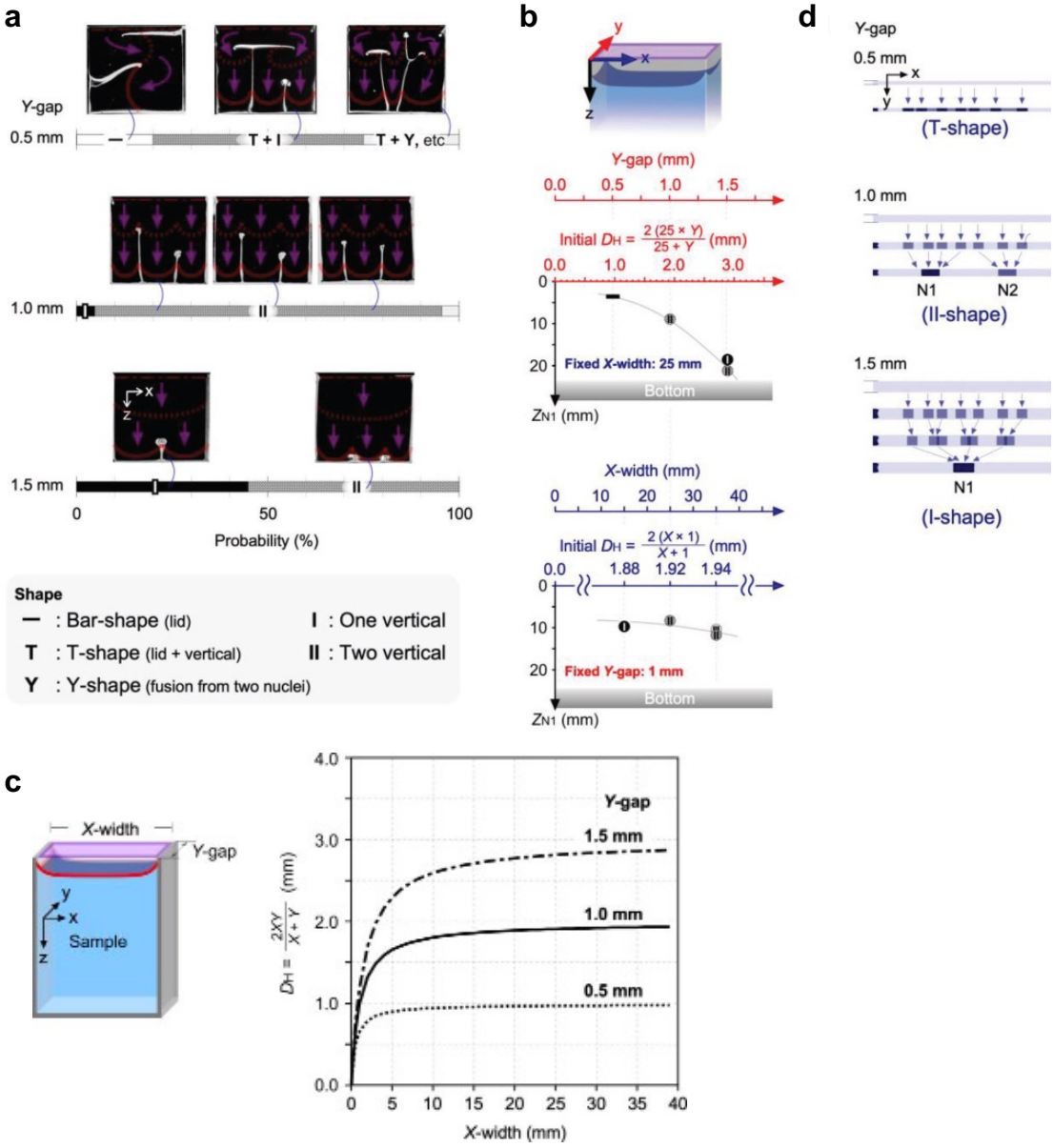

Figure 2.7 a) Images of a typical deposition in cells with a given Y-gap and probability. Cell (25 mm width, Y-gap, 23 mm depth, initial concentration of pectin: 6.0 wt%, drying temperature: 40 °C). 20 trials were conducted. **b)** Effect of the Y-gap in 25-mm-wide cells on the first nucleating Z-position, Z_{N1}. Effect of the X-width in 1-mm-gap cells on Z_{N1}. D_H is the hydraulic diameter calculated using the X-width and Y-gap. Z_{N1} is determined by the statistical average of experimental results from 20 trials. **c)** Correspondence of the cell's X-width and hydraulic diameter D_H at specific Y-gap values. **d)** The schematic of the evaporative interface and nucleation for meniscus splitting.

2.4 Conclusion

In summary, meniscus splitting with multiple nuclei was verified statistically and kinetically based on the parameters of viscous fluids using aqueous pectin dispersions. Multiple nucleations occurred asynchronously in stages following interface fluctuations of the polymer cluster. By controlling the cell width, a statistical analysis specified the two nuclear generations with high probability and the asynchronous trends of the spatial distributions for the first and second nuclei. The spatiotemporal analysis revealed that there existed an induction period for the differentiation of the velocity dZ/dt of the interface, that is, an "interface fluctuation" as a non-equilibrium state between drying and wetting states. This period enabled the recognition of the cell sidewalls as the boundaries and the finiteness of the space for the nucleation in the horizontal X-direction. The evaporative interface formed a wavy shape before depositing a nucleus. This was due to polymer concentration unevenness, which increased the area of the evaporative interface. The system spontaneously achieved dynamic equilibrium and resulted in the dissipation process in the horizontal direction and meniscus splitting. After the interface fluctuation, asynchronous nucleation occurred to generate the first nucleus (not from the center but near the trisection of the cell width), followed by the generation of the second one.

To evaluate the splitting process, the time course of Re was estimated to cause a drastic change in the low range, less than 10^{-6} using the experimental values of ρ, μ, u, and D_H. This methodology will help the application of meniscus splitting in other materials that have inherent physical values. In the future, we will develop a dimensionless model in terms of the dominant parameters such as the capillary number [24] and the Marangoni number. We envision the universalization of this meniscus-splitting phenomenon not only on the millimeter scale but also on the micrometer scale, where geometrically precise structures and systems are generated as microorganisms. This understanding could contribute to designing adaptable microdevices using this technique for material applications.

References

[1] F. Gallaire, P. T. Brun, *Philos. Trans. R. Soc., A*, **375**, 20160155 (2017).

[2] P. G. Saffman, *J. Fluid Mech.*, **173**, 73 (1986).

[3] J. B. Brzoska, F. Brochard-Wyart, F. Rondelez, *Euro phys. Lett.*, **19**, 97 (1992).

[4] K. Okeyoshi, M. K. Okajima, T. Kaneko, *Biomacromolecules*, **17**, 2096 (2016).

[5] K. Okeyoshi, M. K. Okajima, T. Kaneko, *Sci. Rep.*, **7**, 5615 (2017).

[6] K. Okeyoshi, *Polym. J.,* **52**, 1185 (2020).

[7] O. K. Matar, S. M. Troian, *Phys. Fluids*, **11**, 3232 (1999).

[8] Z. Zheng, H. Kim, H. A. Stone, *Phys. Rev. Lett.*, **115**, 174501 (2015).

[9] S. Li, J. S. Lowengrub, J. Fontana, P. Palffy-Muhoray, *Phys. Rev. Lett.*, **102**, 174501 (2009).

[10] E. Tóth-Szeles, Á. Tóth, D. Horváth, *Chem. Commun.*, **50**, 5580 (2014).

[11] K. Okeyoshi, M. Yamashita, T. Sakaguchi, K. Budpud, G. Joshi, T. Kaneko, *Adv. Mater. Interfaces*, **6**, 1900855 (2019).

[12] K. Okeyoshi, M. Yamashita, K. Budpud, G. Joshi, T. Kaneko, *Sci. Rep.*, **11**, 767 (2021).

[13] E. M. Purcell, Am. *J. Phys.*, **45**, 3 (1977).

[14] R. Ajdary, B. L. Tardy, B. D. Mattos, L. Bai, O. J. Rojas, *Adv. Mater.*, **33**, 2001085 (2021).

[15] L. Wu, I. Saito, K. Hongo, K. Okeyoshi, *Adv. Mater. Interfaces*, **10**, 2300510 (2023).

[16] E. Lajeunesse, J. Martin, N. Rakotomalala, D. Salin, *Phys. Rev. Lett.*, **79**, 5254 (1997).

[17] H. Oertel, Prandtl-Essentials of Fluid Mechanics, Springer, New York, NY (2010).

[18] T. Tanaka, S. T. Sun, Y. Hirokawa, S. Katayama, J. Kucera, Y. Hirose, T. Amiya, *Nature*, **325**, 796 (1987).

[19] M. Shibayama, Macromol. *Chem. Phys.*, **199**, 1 (1998).

[20] G. Jing, H. Bodiguel, F. Doumenc, E. Sultan, B. Guerrier, *Langmuir*, **26**, 2288 (2010)

[21] K. Okeyoshi, G. Joshi,M. K. Okajima, T. Kaneko, *Adv. Mater. Interfaces*, **5**, 1701219 (2018).

[22] I. Saito, L.Wu, M.Hara, Y. Ikemoto, T. Kaneko, K.Okeyoshi, *ACS Appl. Polym. Mater.*, **4**, 7054 (2022).

[23] K. Okeyoshi, G. Joshi,M. K. Okajima, T. Kaneko, *Adv. Mater. Interfaces*, **5**, 1701219 (2018).

[24] G. Joshi, K. Okeyoshi, F. A. A. Yusof, T. Mitsumata, M. K. Okajima, T. Kaneko, *J. Colloid Interface Sci.*, **591**, 483 (2021).

Chapter 3

The convection behavior in pectin dispersion during meniscus splitting

3.1 Introduction

Interfacial instability is one of the main reasons for the formation of dissipative structures in soft matter systems,[1] such as coffee ring patterns,[2,3] surface wrinkling,[4,5] and viscous fingering[6,7]. Unlike active matter, which responds to external space, matter, and energy through physicochemical interactions, viscous fluids show great potential for designing delicate biomimetic systems as an intermediate state between fluids and gels.[8–11] For example, in a Hele-Shaw cell composed of two parallel substrates, viscous fluids exhibit various delicate patterns such as finger-like,[12] ring-like,[13] flower-like,[14] branch-like,[15] and schlieren patterns[16] because of their instability under competition from surface tension, capillary effects, and viscous forces.[17,18] Diffusion behavior in the fluid and at the interface may not be synchronized, like the coffee ring,[3,19,20] which hide different mechanisms behind similar patterns. Although numerical simulations have been effectively advancing the study of viscous fingering,[21–24] studies linking the interior behavior of viscous fluids to the interfacial patterns remain poorly understood due to the complexity of phenomena such as Marangoni instability.[25, 26] In particular, the dynamic coupling between internal fluid flow and interfacial behavior during evaporation in viscous fluids remains an important but still underexplored aspect at the frontier of soft matter science, essential for understanding complex pattern formation and interface instabilities.

Building on the concept of viscous dissipation, we extended viscous fingering[12] into a “meniscus splitting” pattern and demonstrated it in aqueous polysaccharides dispersion.[27] By applying thermal energy to an aqueous dispersion in a Hele-Shaw cell with spatial boundaries and inducing water evaporation, the concentrated polymer accumulates, bridging the cell gap at multiple positions. After bridging a gap of approximately 1 mm and generating a deposition nucleus, the dispersed polymer continues to grow into a membrane, leading to the splitting of the evaporative interface.[28,29] As the cell width increases, the number of menisci split by the nucleus

increases at similar intervals. This specific deposition behavior arises from the combined effect of spatial boundaries,[30] water diffusion,[31] and the dynamic integration of mass and heat transfer. Splitting patterns that flocculate at specific positions have been observed in some aqueous polymers, and the deposited polymer membranes exhibit oriented nanostructures and microlayer structures.[32–35] However, the critical role of "skin layer" and its growth during initial polymer densification on the evaporative interface remains unclear. During the process of continuous thermal energy supply, interface fluctuations lead to meniscus splitting. Previous reports have focused only on the finite interface, without exploring the contribution of the finite liquid phase.[36] Therefore, understanding the mass flow within the finite liquid phase is essential to determine the unique spatiotemporal ordering of polymer accumulation that leads to interfacial fluctuations.

In this study, we elucidated the underlying mechanism of specific polymer accumulation in meniscus splitting by considering the characteristic Marangoni circulations in the fluid during the nonequilibrium period. Using aqueous pectin dispersion with high viscosity as an example of a non-Newtonian fluid, we accurately monitored the emergence and evolution of Marangoni convection in the finite liquid phase (**Figure 3.1**). Here, the quasi-two-dimensional Marangoni convection beneath the evaporating interface is characterized by multiple mass circulations, particularly with confluence and bifurcation regions that correspond to interfacial fluctuations. To clarify the fluid motion, a kinetic study was conducted using the particle image velocimetry (PIV) method. Through this approach, we revealed the relationship among the flow directions, nucleus positions, and spatio-temporal development.

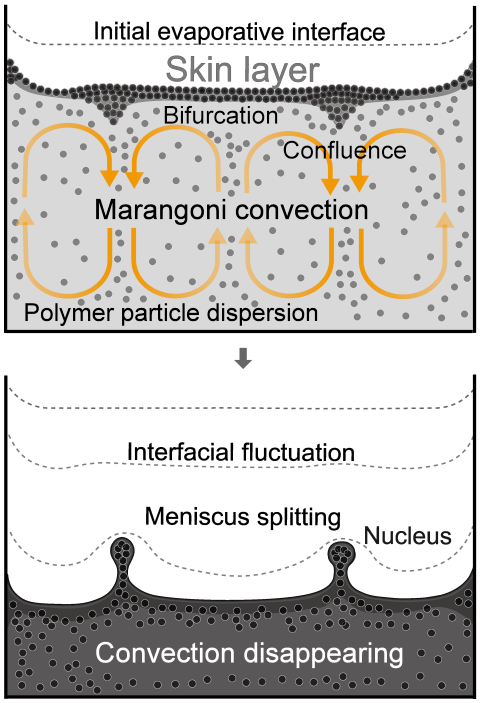

Figure 3.1 Nonequilibrium period with emergence of Marangoni convection in meniscus splitting. During the interfacial fluctuation process before meniscus splitting, Marangoni flow is induced as quasi-two-dimensional convection in aqueous polymer dispersion. Polymer particles integrate on the evaporative interface and the skin layer grows with deformation to form multiple deposited nuclei. Convection disappears while the meniscus splitting continues (bottom diagram). The schematic model shows the aqueous dispersion of polymer particles in the Hele-Shaw cell.

3.2 Experimental

3.2.1 Materials

Citrus pectin with a molecular weight in the range of 20–400 kDa was purchased from Nacalai Tesque, Japan. Low-methoxy pectin contained more than 50% galacturonic acid units and 11% methoxy groups. The pectin powder was dispersed in pure water at room temperature. The aqueous pectin dispersion was stored in a refrigerator and used within one week to prevent property changes. A polystyrene divinylbenzene copolymer microsphere suspension, purchased from Thermo Fisher Scientific, with a specific density of 1.05 g/cm^3, was used as a tracer particle for PIV analysis. The mean diameter of the particles was 12 μm with a size distribution ≤ 18% coefficient of variation. To measure the skin layer thickness, a polystyrene microsphere suspension, purchased from Thermo Fisher Scientific (1.05 g/cm^3 density, mean diameter of 1.1 μm, size distribution ≤ 3% coefficient of variation) was used to enhance the visibility of the concentration gradient (Figure S1, Supporting Information). Each suspension was dispersed in the prepared aqueous pectin dispersion at a volume fraction of 0.5 vol.% after a brief (15 s) immersion in a low-power ultrasonic bath (at 28kHz). The Hele-Shaw cell (X-width, Y-gap, and Z-depth) was composed of two nonmodified glass slides and U-shaped polyvinyl chloride spacers with the required thickness (0.5, 1.0, 1.5, and 2.0 mm). Nonmodified glass substrates were purchased from Matsunami Glass Ind. Ltd., Japan.

3.2.2 Drying experiment

After removing minor amounts of impurities and air bubbles through centrifugation (6000 rpm, 15 s), the dispersion was filled in the top-open Hele-Shaw cell to avoid the deposition of tracer particles. The drying experiment was carried out in a drying observation box at a controlled temperature and atmospheric pressure maintained using an air circulator, as previously reported [34]. During drying, the samples were monitored through glass windows and images were captured using a Canon EOS kiss X10.

3.2.3 Surface tension measurement

The surface tensions of the liquids were measured using a Dropmaster DM401 (Kyowa Interface Science Co., Ltd.). Temperature and humidity were controlled in a box using heating and cooling hardware and a humidity controller (Kyowa Interface Science Co., Ltd.). The droplets were set on the injection needle using a syringe with ~10.0 μL for each drop. To avoid evaporation during measurement, the humidity was controlled at >90% by shutting off the air circulation and closing the box windows under constant temperatures (40, 50, and 60 °C). The change in surface tension of the slow droplet evaporation for 600 s at different temperatures was measured as shown in **Figure 3.2**.

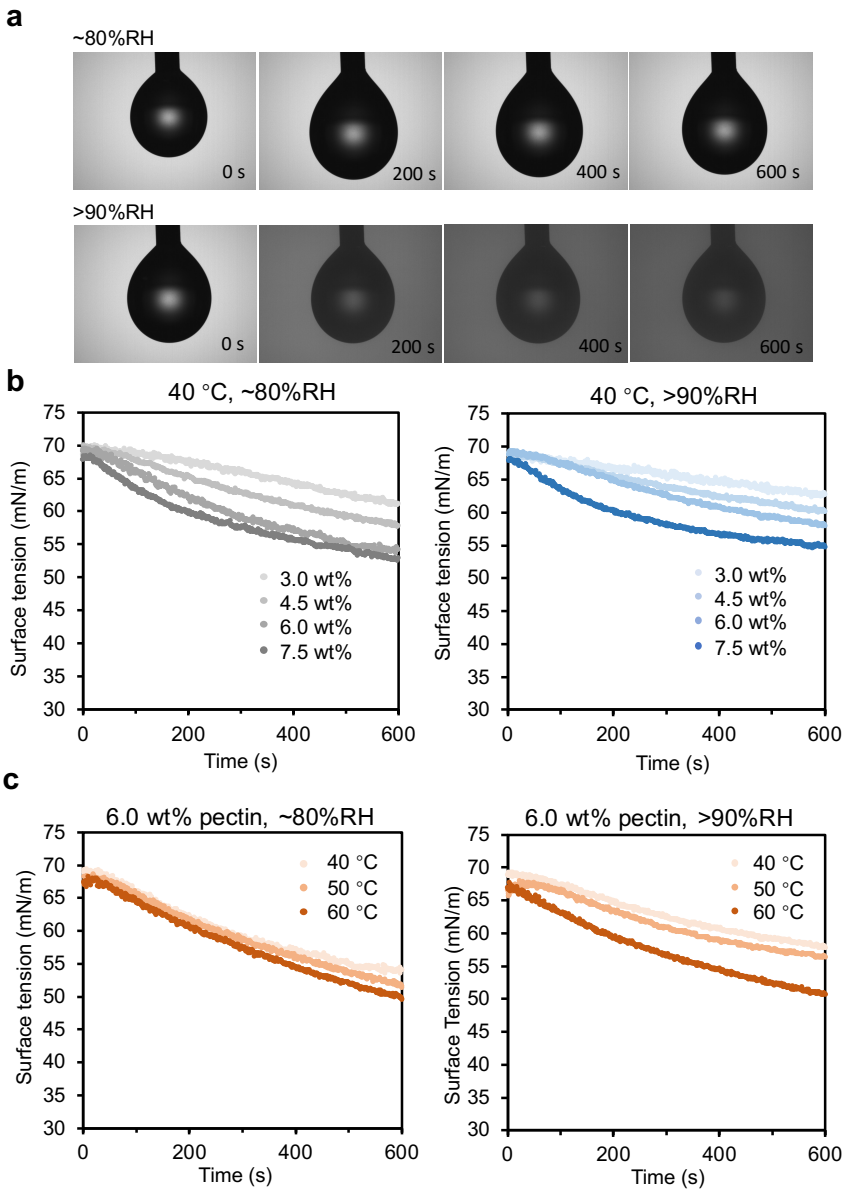

Figure 3.2 Surface tension of pectin dispersion during time measured by pendant drop method. a) Snapshots of surface tension measurement (take 3.0 wt% pectin at 40 °C as an example, controlling humidity at ~80% RH and humidity >90% RH respectively). At high humidity without circulated air control, the background of the screen is darkened because of water vapor condensation in front of the observation glass. **b)** Surface tension measured at 40 °C with controlled humidity of ~80% RH (left), and >90% RH (right). **c)** Surface tension of 6.0 wt% pectin dispersion measured at different temperatures with controlled humidity of ~80% RH (left) and >90% RH (right).

3.2.4 Image analysis

Particle image velocimetry (PIV) analysis was performed on 8-bit images obtained during the drying experiment (10 min frame interval) using PIVlab in MATLAB.[37] Before analysis, the image sequences were cropped into a region of interest to fit the size of Hele-Shaw cells and preprocessed using the contrast-limited adaptive histogram equalization value of 64 pixel with auto contrast stretch. Image pairs (A–B and B–C) were cross-correlated to extract the local displacement between two frames based on the fast Fourier transforms (FFT) window deformation algorithm. The size of the interrogation area was 128 × 128 pixel, followed by two passes with half the step of the previous size. The last pass was repeated until the quality slope was < 0.025. A Gaussian 2 × 3 fit was used for the subpixel accuracy with high correlation robustness. The drying experiment was compiled into a video with a magnitude display and a suitable scale bar.

Interfacial behaviors were analyzed by image sequences in drying experiments using the ImageJ software (National Institutes of Health, Bethesda, MD, USA). A stack of images was obtained every 10 min to demonstrate the interfacial behavior under different conditions. The spatiotemporal analysis of the interfacial motion speed was performed by reslicing the image sequences of the given interfacial positions in the nucleation positions and center of the emerged meniscus during evaporation (M1, N1, M2, N2, and M3). The Z-position of the interface was plotted using a GetData Graph Digitizer. The interfacial speed (dZ/dt) was estimated using Z-position plots. The speed of the tracer particles was also manually extracted for careful analysis of the convection behavior in the outer loop

regions. The path of particle motion was determined by stacking every 100 min (at 10 min intervals, 11 images), and the speed (dZ/dt) was plotted every 100 min.

The skin layer is based on the boundary layer at the air–liquid interface during evaporation. To measure the thickness of the skin layer, the change in the transmitted light intensity before nucleation at 1800 min was calculated using the gray-scale values corresponding to the given X-positions. The gray-scale values corresponding to the X-positions were obtained at different Z-depths from the 8-bit images using ImageJ software. To reduce background interference, image sequences were compared based on the gray-scale ranges. Manual measurements were conducted three times and the averages were plotted with corresponding error bars indicating the standard deviation.

3.3 Results and discussion

3.3.1 The emergence and evolution of Marangoni convection patterns

The demonstrations were carried out by using aqueous pectin dispersion (M_w < ~ 400 kDa, 6.0 wt%, ~ 1000 mPa•s at 40 ℃, dispersed microparticles of approximately 1 μm diameter).[36] To investigate the assembly behavior in the liquid phase during evaporation, the evaporation process was visualized from the initial dispersion to the deposited pattern at the microscale using the PIV analysis. The addition of tracer particle with diameter of 12 μm did not disrupt meniscus splitting. Consequently, we successfully observed the emergence of an ordered Marangoni convection pattern over a long timescale. The flow evolution that occurs in the liquid phase is observed in the stacked images of the drying process (**Figure 3.3a**). The air–liquid interface split from the initial meniscus into three menisci, mediated by the deposited nuclei during evaporation, whereas convection was accompanied by initial evaporation and flocculating nucleation. The velocity-field distribution in the liquid phase can help in the understanding of the convective behavior at the corresponding time (**Figure 3.3b**). To describe the characteristic positions at the air–liquid interface, the centers of the meniscus were marked as M1, M2, and M3, and the nucleation positions were designated as N1 and N2. From the initial time to ~ 300 min, the initial evaporation induced a concentration gradient near the two top concaves, which caused two Marangoni flows from the two sidewalls toward the center. Separately, to enhance visual contrast, 1.1 μm particle were added, enabling clearer visualization of the concentration gradient. These observations suggest that the initial evaporation induced the concentration gradient near the two top concaves, which caused two Marangoni flows from the two sidewalls toward the center.

Detailed investigations of the flow revealed that particle speeds were not homogeneous in the liquid phase. We measured the speed of the outer circulation over the liquid as the characteristic speed and compared the motion of the particles at the N1 and M2 interfacial positions (**Figure 3.3c**). The speed of the evaporative interface at N1

indicated flocculation of the polymer dispersion, whereas that at M2 indicated the evaporation speed. During the initial period (0–100 min), the evaporative interface decreased rapidly; however, the flow speed within the internal liquid remained relatively unchanged. However, after 200 min, the particles in the liquid accelerated and gradually developed into circulation, whereas the speed of the evaporating interface increased with the perturbation. From 300 to 600 min, the Marangoni flows beneath the evaporation interface merged into plumes and accelerated, which expanded directly toward the bottom. Here, the higher-density upper layer pushed the lower-density viscous fluid downward, causing circulation in the liquid phase.[38] After 600 min, the plumes reached the bottom and the spatial periodic convection expanded to occupy the entire liquid phase, which dominated the mass flow within the dispersion. The concentration gradient between the upper and bottom liquids decreased as the circular flow continued, which gradually decreased between 600–1200 min. During this period, interfacial fluctuations at the evaporative interface become more significant, as shown in the stacked images in Figure 3.3c. The dispersed polymers at the air–liquid interface accumulated and flocculated into nucleation at ~ 1800 min. Although evaporation continued during nucleation, the mobility of the particles in the liquid gradually decreased, and the particles nearly disappeared after 2400 min. This finding indicates that the dispersion was too concentrated and viscous to facilitate the movement of particles.

After nucleation, the polymer particles in the dispersion were integrated in an orderly manner at the evaporative interface owing to the capillary effect. Notably, the process of convection emergence and evolution is a significant nonequilibrium period for meniscus splitting. Therefore, Marangoni flow was induced by the initial evaporation rising from the two sidewalls, and quasi-two-dimensional circulations were formed in the cell. To enhance the visual contrast, 1.1 μm particles were added to enable the clearer visualization of the concentration gradient (**Figure 3.3d**). Circulations carried the particles to specific positions beneath the evaporative interface to enhance the interfacial fluctuation. Notably, the flow direction was downward at the nucleation positions,

whereas it was upward at the central position of the emerged meniscus. We confirmed that the water evaporation was necessary for the flow generation by carrying out a control experiment with a liquid paraffin layer to inhibit the evaporation (**Figure 3.3e**). When the liquid paraffin existed between the aqueous polymer dispersion and the air, the mass flow could not be observed. This means that the water evaporation substantially induces the mass flow of the polymer dispersion.

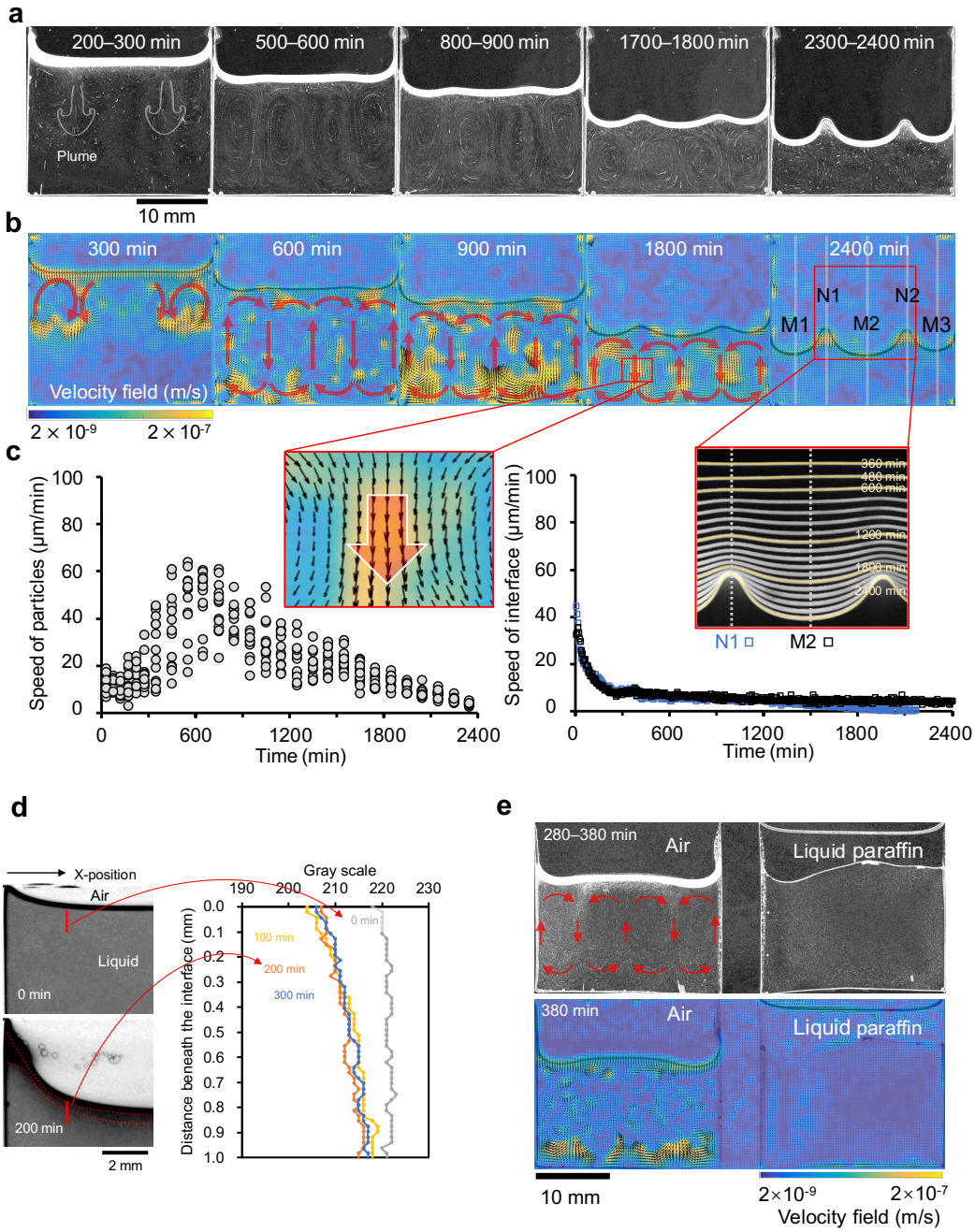

Figure 3.3 Emergence of Marangoni circulation prior to meniscus splitting and time evolution. a) Stack images of convection emergence at given periods: 200–300 min, 500–600 min, 800–900 min, 1700–1800 min, and 2300–2400 min. **b)** Particle image velocimetry images of internal flow showing the vector of tracer particles in liquid phase at given time: 300, 600, 900, 1800, and 2400 min. The velocity field is shown by blue and yellow colors in the background. **c)** Characteristic speed of tracer particles at outer convections (left) and interfacial motion speed at nucleation position N1 and central meniscus M2 (right). Sample: 6.0 wt% pectin aqueous dispersion including tracer particle drying at 40 °C. Cell (25 mm-width, 1 mm-gap, 23 mm-depth).

d) The snapshots of evaporative interface at 0 min and 200 min. Concentration gradients develops beneath the air-liquid interface during evaporation, highlighted using 1.1 μm particles for better visualization. **(b)** The concentration gradient reflected in the gray scale values at the given X-position at 0 min, 100 min, 200 min and 300 min. **e)** Internal flow under evaporation and evaporation-inhibited conditions. Stack image (280–380 min) and the PIV velocity field image (at 380 min) show that internal convection emerged in the evaporating sample, while no significant flow behavior was observed under conditions where evaporation was inhibited by a liquid paraffin layer. Initial concentration of pectin dispersion: 6.0 wt%; cell size: 25 mm-width, 1 mm-gap, 23 mm-depth, evaporation temperature: 40 ℃.

3.3.2 Effect of initial concentration and evaporation temperature

The evolution of interfacial fluctuation during splitting is summarized in **Figure 3.4a**. clearly shows the growth of the interfacial fluctuation and Marangoni pattern, depending on the initial polymer concentration and drying temperature. As the initial concentration increased, the number of nuclei increased from one nucleus at 3.0 wt% to two nuclei at 6.0 wt%. However, at 4.5 wt%, an intermediate behavior was observed, where two nuclei fluctuated during the initial period, but eventually, only one nucleus was deposited and bridged the gap. This fact in concentration indicates that interfacial fluctuation and the nucleation are related to the localized concentration process. During the denser period at the interface, the polymer clusters in the flow were deposited at multiple positions. As the temperature and evaporation rate increased, the viscosity of the polymer dispersion decreased.[36] A higher evaporation rate facilitated polymer deposition on the glass substrates. In contrast, a decrease in viscosity enabled the polymers to slip readily in the dispersion rather than in the viscosity-limited capture at specific positions. Therefore, deposition nucleation at 60 ℃ was slower than that observed at 40 ℃.

The evaporative interface plays a crucial role as a flexible open boundary for water discharge into air during interfacial deformation and characteristic mass flow in the liquid phase. As shown in **Figure 3.4b**, the motion of the multiple plumes at the two downward confluences can be observed at C_0 = 4.5 wt% and 50 ℃. The polymer particles were concentrated at the confluence to form plumes that appeared as dark shadows. The confluence was then directed toward the bottom owing to the concentration gradient. During the 5–10 h period, three plumes in competitive positioning were observed. The two became closer to merging and the mass circulation between them disappeared. From the start to the end of the competition, the evaporative interface was flexible owing to the relaxation of surface tension. At 20–40 h, the two plumes from the three survived; one became the deposition nucleus, and the other behaved as a pre-nucleus until it was completely dried. The process clearly exposed the nonequilibrium period from the interfacial fluctuation to meniscus splitting. The emergence of confluence is related to

convective instability, which exhibits the properties of particle trapping.[39] However, considering that other polymer, such as xanthan, did not show any mass flow in the liquid phase, but instead showed meniscus splitting in 50 mm-depth cells.[40] The Marangoni circulation is not the only reason for meniscus splitting; other factors, such as capillary instability,[41] are also considered to contribute to the meniscus splitting.

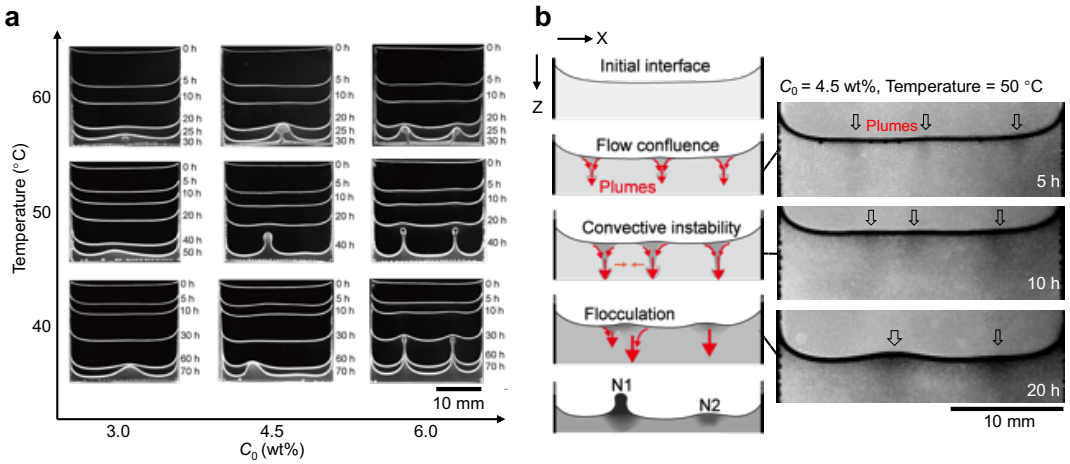

Figure 3.4 Interfacial fluctuation with merging of flow confluences. a) Time course changes at air–liquid interface and effect of initial pectin concentration C_0 and drying temperature. Interfacial evolution is shown by stacked images corresponding to characteristic times. Cell size (25 mm-width, 1 mm-gap, and 23 mm-depth). **b)** Schematic of flow confluence merging and actual images of multiple plumes generation/merging process around the evaporative interface. Sample: 4.5 wt% pectin dispersion drying at 50 °C.

3.3.3 The formation and reorganization of skin layer at the interface

During evaporation, the accumulated polymer at the air–liquid interface gradually became saturated and supersaturated. This situation leads to the formation of a concentrated polymer layer beneath the evaporative interface, as the skin layer.[42] The thickness of the skin layer can be used to characterize the process of polymer accumulation at the interface. As shown in **Figure 3.5a**, the gray values from snapshots of meniscus M1 provide insight into the skin layer formation, exhibiting a sharp peak and tail. The sharp peak indicates a curved meniscus between the substrates in the Y-gap direction parallel to the light direction, appearing nearly black. The tail region represents the skin layer. As the concentrated dispersion exhibited lower light transmittance, the thickness of the skin layer was measured before nucleation (~ 1800 min). To minimize the interference of pixel noise from the background, such as the glass substrate and scattered light that changes with the camera view, the thickness of skin layer was measured manually by comparing the real-time image sequence frame-by-frame. The gray value of each pixel at the given positions (M1, N1, M2, N2, and M3) was analyzed using the ImageJ software to determine the thickness of the skin layer. A stack of snapshots revealed the particle trajectories beneath and within the skin layer (**Figure 3.5b**). Compared to the thickening speed of the skin layer at nuclei positions N1 and N2, those at meniscal positions M1 and M3 were smaller. This difference indicated that the interface was enlarged at M1 and M3 for water evaporation. Notably, the thickening speed of meniscus M2 was similar to those at N1 and N2 before 600 min, but it slowed down in the 900–1800 min period, demonstrating a similar speed as the menisci positions at M1 and M3. Therefore, the stepwise deformation of the skin layer originated from convection reordering in the liquid.

Figure 3.5c shows the deformation of the skin layer, accompanied by convection. The Marangoni flow near the sidewalls initially sheared M1 and M3, causing a confluence to merge into the plumes. After the plumes reached the bottom of the cell, the deformation of the skin layer was accelerated owing to squeezing at the confluence positions and

tearing at the bifurcation positions. The polymer particles accumulated around the pre-nuclei driven by repulsive plumes and bridged the gap through evaporation. Following nucleation, the concentration gradient decreased because the concentration was mostly saturated over the entire volume, leading to the disappearance of convection. Simultaneously, the skin layer of approximately 1.5 mm was less affected by the shear inertia of convective flow,[43] which facilitated stable polymer accumulation in the nuclei. During later meniscal splitting, the capillary force near the nuclei was dominant. Therefore, periodic deposition can be explained from the viewpoint of dispersion concentration.

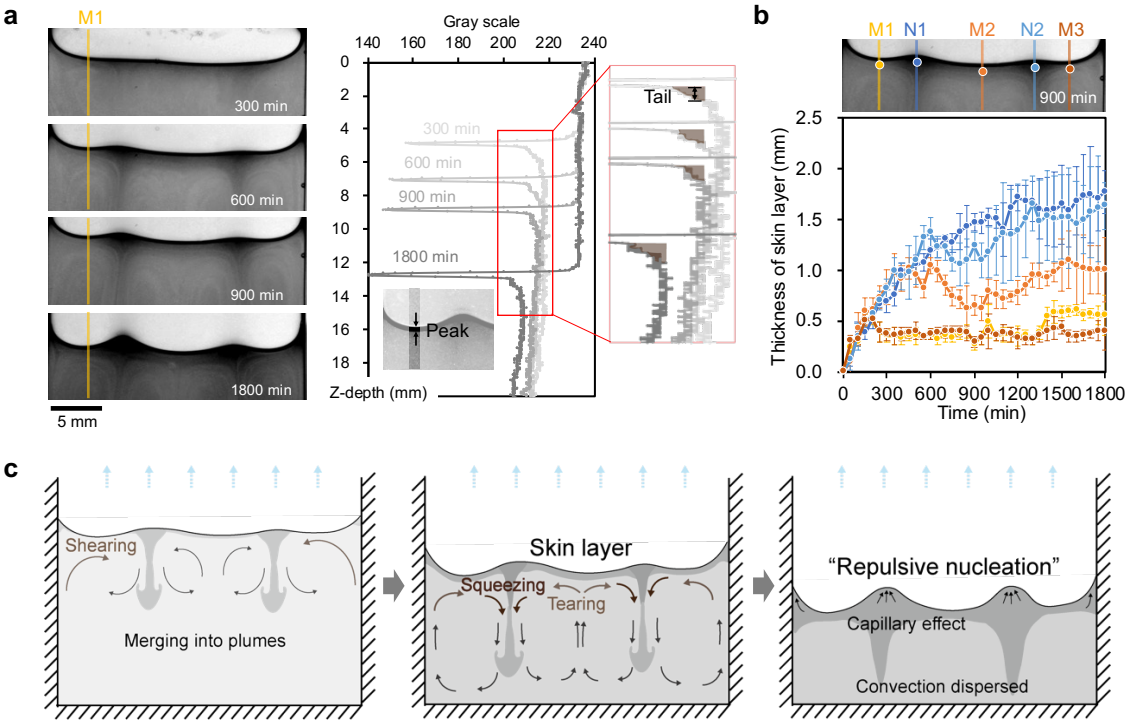

Figure 3.5 Growth and deformation of skin layer at evaporative interface. a) Snapshots of skin layer at a given time. Initial pectin concentration: 6.0 wt%, 1.1 μm particles was added to enhance the visualization. Cell size: 25 mm-width, 1 mm-gap, 23 mm-depth. Evaporation temperature: 40 °C. Peaks of gray values extracted from the M1-position indicate air–liquid interface, and the color region below peak is recognized as the skin layer. **b**) Time course of skin layer thickness at M1, N1, M2, N2, M3 before nucleation. **c)** Schematic of skin layer growth and deformation in meniscus splitting.

3.3.4 Capillary effect and Marangoni effect

To investigate the capillary effect during the initial process, drying experiments were conducted using cells with different Y-gap. The different deposition patterns were exhibited with similar evaporation speed (**Figure 3.6a**). Unlike the deposition from the cells with a 1.5 or 2.0 mm gap, vertical membrane bridging the gap was observed for polymer deposition from the cells with a 0.5 or 1.0 mm gap. Considering that the typical capillary length was in the range of 2–3 mm for the air–water interface,[44] a Y-gap of approximately half this length (1.0–1.5 mm) is critical for dispersion between two parallel substrates. Notably, the flow in the cell with a 0.5 mm gap differed substantially quantitatively and qualitatively from that in the 1.0 mm gap (see Figure 3.6a). In the 1.0 mm gap, the convection pattern formed four ordered circulations with nucleation occurring above the downward confluences. In contrast, the 0.5 mm gap exhibited two localized circulations, with nucleation occurring above the upward flow as the fluid moved toward the nucleus. The speed of internal flow was compared by analyzing the motion of tracer particles (**Figure 3.6b**). The characteristic speed at 600 min in the 1.0 mm gap was approximately 50 μm/min, and that in the 0.5 mm gap was significantly slower, approximately 10 μm/min. By simply reducing the gap by half, the internal mass flow and nucleation process changed drastically, capillary effects play a dominant role here.

Interfacial curves were analyzed to study the pressure difference in the air–liquid interface during the nonequilibrium period.[45] As shown in **Figure 3.6c**, the air–liquid interface exhibits interfacial curves in the X-width and Y-gap directions corresponding to radii R_x and R_y, respectively. Considering the interface curve as an arc of radius R_y, it can be obtained using the Pythagorean Theorem expressed by equation (1),

$$(R_y - h)^2 + (\frac{Y}{2})^2 = {R_y}^2 \qquad (1)$$

where h is the height of the air–liquid interface and Y is the length of the Y-gap. h can be measured from the side views. According to the time course image of h, that of R_y during

polymer accumulation is useful for expressing surface tension (**Figure 3.6d**). During evaporation R_y remains relatively stable within the same cell but varies significantly for different Y-gaps. Based on the measured γ (68 mN/m at 40 °C) and R_y, the pressure difference ΔP as a function of R_x can be expressed using the Young–Laplace equation expressed by equation (2).

$$\Delta P = \gamma \left(\frac{1}{R_x} + \frac{1}{R_y} \right) \qquad (2)$$

As shown in **Figure 3.6e**, ΔP in the 0.5 mm gap is remarkably larger than those in other gaps (1.0, 1.5, and 2.0 mm gaps). The particles, as well as the dispersion, were driven toward the evaporation interface by capillary pressure (200–300 N/m^2) between the substrates and deposited to bridge the gap. As the gap of the cell increased, the capillary pressure decreased, and the surface tension gradient in the liquid gradually became dominant, resulting in the emergence of Marangoni convection patterns. To clarify the relationship between the capillary effect and Marangoni convection, dimensionless numbers were compared. The capillary number, *Ca* as the ratio of the fluid viscous force to the surface tension, is calculated using equation (3),

$$Ca = \frac{\mu v}{\gamma} \qquad (3)$$

where μ is the viscosity, v is the characteristic speed, and γ is the surface tension. Based on the differences observed (Figure 3.6a-b), comparing particle motion between the cells with 0.5 and 1.0 mm gaps is particularly interesting. Using experimental conditions of 6.0 wt%, pectin dispersion at 40 ℃, μ of 1120 mPa•s, γ of 68 mN/m, the *Ca* in the 1.0 mm gap of the evaporation interface was approximately 10^{-6} and that of the internal fluid in convection was approximately 10^{-5}. In contrast, in the 0.5 mm gap, both were approximately 10^{-6}. Due to the viscosity increase with evaporation, the actual *Ca* should be much higher than this value. These estimations suggested that the critical value of *Ca* for the nonequilibrium period should be > 10^{-6}.

Considering the emergence and disappearance of convection, the Marangoni number, *Ma* as the ratio of the transport due to Marangoni flows, with the rate of transport of diffusion is shown as equation (4).

$$Ma = \left(\frac{\partial \gamma}{\partial C}\right) \frac{\Delta C L}{\mu D} \qquad (4)$$

Where γ is the surface tension, *C* is the concentration, *L* is the characteristic length, and *D* is the diffusion coefficient. The surface tension of pectin dispersion was evaluated with different concentration and temperature by pendant drop method with controlled temperature and humidity. The concentration gradient ($\partial\gamma/\partial C$) affects surface tension more than temperature gradient ($\partial\gamma/\partial T$), even with slight evaporation. This result is consistent with the interpretation that convection emerged with the flow from high concentration regions showing low surface tension to low concentration regions showing high surface tension.[46] Here, the Marangoni number, which is used to describe convection behavior, represents the combined effects of solutal and thermal gradients during evaporation.

Due to the difficulty in the quantitative evaluation of the concentration during evaporation, the Marangoni effect is described by the convection flow speed. The ratio of *Ma* to *Ca* is proposed to describe the competition of capillary effect and Marangoni effect, shown as equation (5).

$$\frac{Ma}{Ca} = \frac{\Delta \gamma^2 L}{\mu^2 v D} \qquad (5)$$

By this equation, *Ma*/*Ca* emphasizes the competition between surface tension and viscous force. The characteristic fluid behavior (V_{flow}/V_{evap}) provides an experimental interpretation for the *Ma*/*Ca*, which is defined as the ratio between the internal flow speed and the evaporation interface speed as shown in **Figure 3.6f**. The ratio of the internal flow speed and evaporation interface speed (V_{flow}/V_{evap}) in cells with 0.5 and 1.0 mm gap represent the characteristics fluid behaviors dominated by viscous force and surface tension, respectively. In the 0.5 mm gap, the V_{flow}/V_{evap} fluctuates around 1, indicating

that the speed of particles in the fluid is comparable to that of the evaporation interface. This suggests that the fluid speed is comparable to the interface speed, and the viscous forces dominate the fluid behavior in the cell with 0.5 mm gap. In contrast, in the 1.0 mm gap with a lower Laplace pressure condition, the characteristic fluid behavior shows a gradual increase process after the initial evaporation. After 300 min, the V_{flow}/V_{evap} became larger than 1, indicating the contribution of Marangoni effect, where the fluid behavior becomes dominated by surface tension. Owing to the high viscosity after nucleation deposition after 2400 min, the fluid behavior reverts to viscosity-dominated, with V_{flow}/V_{evap} returning to approximately 1. Thus, the time course changes in the fluid behaviors in different cell gaps clearly indicate the competitive condition between the surface tension and viscous forces during meniscus splitting.

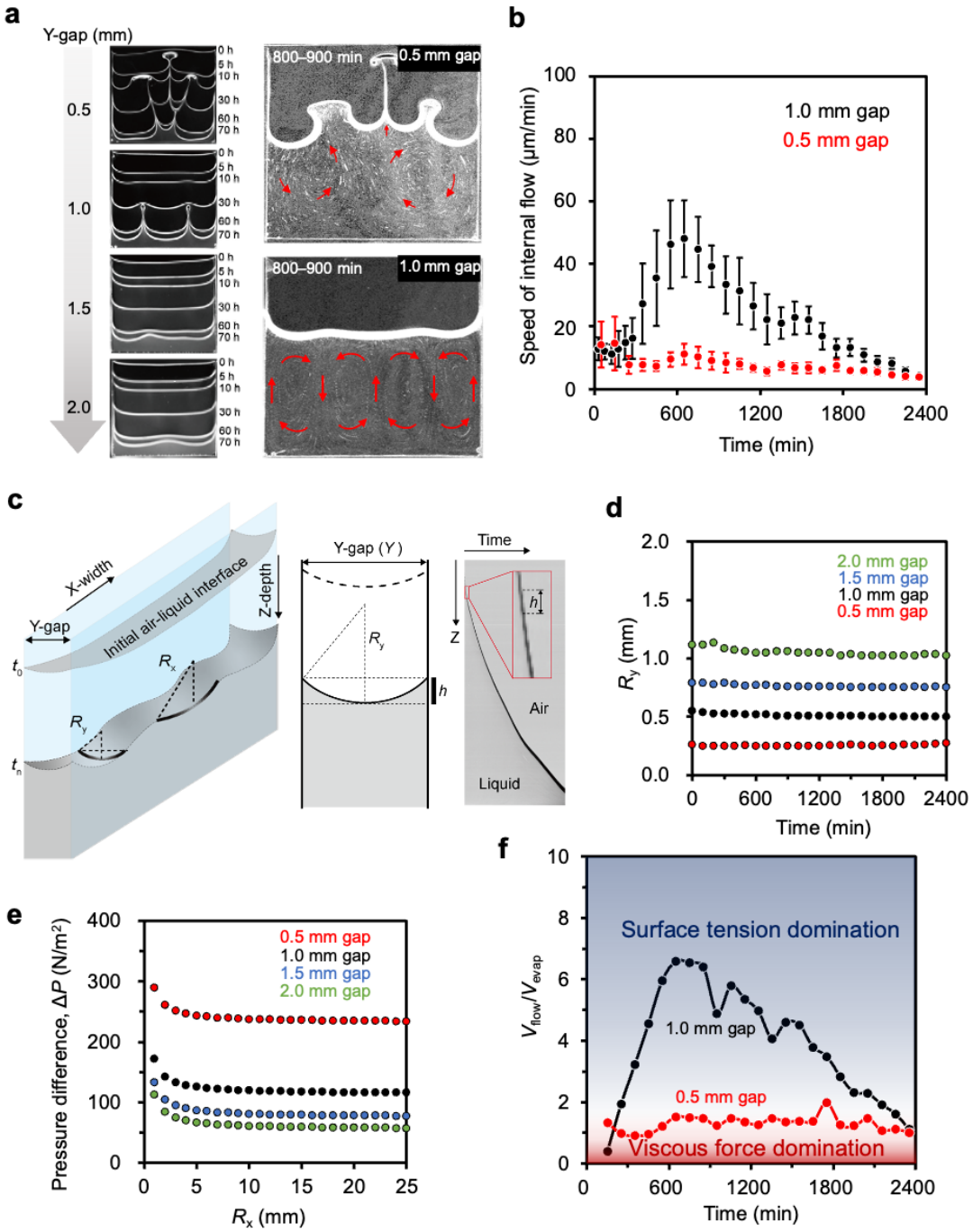

Figure 3.6 The competition between capillary effect and Marangoni effect. a) Stack images of evaporative interface and liquid phase in given cell gap size. Cell size (25 mm-width, Y-gap, 23 mm-depth). Initial pectin concentration: 6.0 wt%. Drying temperature: 40 °C. Red arrows indicate the directions of tracer particles. **b)** Time course of the internal flow speed in cells with 0.5 and 1.0 mm gap. **c)** Schematic of interfacial curves in directions of X-width and Y-gap. R_x and R_y represent the radius of curvatures in each direction. The right image is time course curve prepared from the sequence of the snapshots with fixed X-position, where the black line indicated the air–

liquid interface a downward meniscus with R_y is generated. The black pixel height is indicated as h. **d)** R_y as a function of time, calculated from the height of meniscus interface, h. **e)** Pressure difference as a function of R_x calculated from the Young–Laplace equation. **f)** The ratio of internal flow speed and evaporation speed (V_{flow}/V_{evap}) in cells with 0.5 and 1.0 mm gap.

3.4 Conclusion

The nonequilibrium period associated with the emergence of Marangoni convection was successfully captured during the meniscus splitting of the aqueous pectin dispersion. The continuous supply of heat energy induced fluctuations in the fluid system at the evaporative interface and drove the mass flow within the Marangoni circulation. During the initial process of water evaporation, the flow started from the two sidewalls because of the capillarity of the space boundaries. Experimental observations revealed that multiple circulations formed in an ordered manner, leading to the emergence of confluences and bifurcations beneath the dense polymer skin layer. During the fluctuation period before nucleation, the two confluence points merged into one point to form one nucleus. This finding highlights the role of Marangoni convection in ordering viscous dispersions and demonstrates its potential for guiding pattern design. The estimation of the characteristic internal flow and Laplace pressure difference at the evaporative interface also supported that the capillary effect was dominant for generation of the ordered splitting. In near future, the splitting phenomena would be comprehensively understand including polymer dispersion systems with/without mass convection, accompanied with infinitesimal thermal variations. The splitting method using the capillarity in this study will also provide a strategy for the colloidal self-assembly and preparation of anisotropic soft materials.[27,34,35] Such physical demonstrations would provide a foundation for predicting hydrodynamic phenomena using advanced numerical simulation and mathematical methods.

References

[1] R. Mukherjee, A. Sharma, *Soft Matter* **2015**, *11*, 8717.
[2] W. Han, Z. Lin, *Angew. Chem. Int. Ed.* **2012**, *51*, 1534.
[3] P. J. Yunker, T. Still, M. A. Lohr, A. G. Yodh, *Nature* **2011**, *476*, 308.
[4] J. H. Na, S. U. Kim, Y. Sohn, S. D. Lee, *Soft Matter* **2015**, *11*, 4788.
[5] Y. Zhang, Y. Qian, Z. Liu, Z. Li, D. Zang, *Eur. Phys. J. E* **2014**, *37*, 1.
[6] P. G. Saffman, G. I. Taylor, *Proc. R. Soc. Lond. A* **1958**, *245*, 312.
[7] T. T. Al-Housseiny, P. A. Tsai, H. A. Stone, *Nat. Phys.* **2012**, *8*, 747.
[8] A. D. C. Nguindjel, P. J. de Visser, M. Winkens, P. A. Korevaar, *Phys. Chem. Chem. Phys.* **2022**, *24*, 23980.
[9] O. E. Shklyaev, A. C. Balazs, *Nat. Nanotechnol.* **2024**, *19*, 146.
[10] K. Zhang, Q. Feng, Z. Fang, L. Gu, L. Bian, *Chem. Rev.* **2021**, *121*, 11149.
[11] M. Peydayesh, S. Kistler, J. Zhou, V. Lutz-Bueno, F. D. Victorelli, A. B. Meneguin, L. Spósito, T. M. Bauab, M. Chorilli, R. Mezzenga, *Nat. Commun.* **2023**, *14*, 1848.
[12] J. B. Brzoska, F. Brochard-Wyart, F. Rondelez, *Europhys. Lett.* **1992**, *19*, 97.
[13] V. K. Vlasko-Vlasov, M. Sulwer, E. V. Shevchenko, J. Parker, W. K. Kwok, *Phys. Rev. E* **2020**, *102*, 052608.
[14] F. Wodlei, J. Sebilleau, J. Magnaudet, V. Pimienta, *Nat. Commun.* **2018**, *9*, 820.
[15] D. Zhang, J. M. Campbell, J. A.Eriksen, E. G. Flekkøy, K. J.Måløy, C. W. MacMinn, B. Sandnes, *Nat. Commun.* **2023**, *14*, 3044.
[16] D. M. Escala, A. P. Muñuzuri, *Sci. Rep.* **2021**, *11*, 24368.
[17] F. Gallaire, P. T. Brun, *Philos. Trans. R. Soc. A* **2017**, *375*, 20160155.
[18] S. W. McCue, *J. Fluid Mech.* **2018**, *834*, 1.
[19] H. Almohammadi, Y. Fu, R. Mezzenga, *ACS Nano* **2023**, *17*, 3098.
[20] H. Hu, R. G. Larson, *J. Phys. Chem. B* **2006**, *110*, 7090.
[21] E. Lauga, A. M. Davis, *J. Fluid Mech.* **2012**, *705*, 120.
[22] F. Gallaire, P. Meliga, P. Laure, C. N. Baroud, *Phys. Fluids* **2014**, *26*, 062105.
[23] M. Mokbel, K. Schwarzenberger, K. Eckert, S. Aland, *Int. J. Heat Mass Transf.* **2017**, *115*, 1064.
[24] Y. Li, J. G. Meijer, D. Lohse, *J. Fluid Mech.* **2022**, *932*, A11.
[25] K. Schwarzenberger, T. Köllner, H. Linde, T. Boeck, S. Odenbach, K. Eckert, *Adv. Colloid Interface Sci.* **2014**, *206*, 344.
[26] M. Winkens, P. A. Korevaar, *Langmuir* **2022**, *38*, 10799.
[27] K. Okeyoshi, *Polym. J.* **2020**, *52*, 1185.
[28] K. Okeyoshi, M. K. Okajima, T. Kaneko, *Sci. Rep.* **2017**, *7*, 5615.
[29] K. Okeyoshi, M. Yamashita, K. Budpud, G. Joshi, T. Kaneko, *Sci. Rep.* **2021**, *11*, 767.
[30] T. K. L. Nguyen, T. Hatta, K. Ogura, Y. Tonomura, & K. Okeyoshi, *Adv. Sci.* **2025**, e03807.
[31] R. Hagiwara, K. Okeyoshi, *STAM*, **2025**, *26*, 2512704.

[32] K. Okeyoshi, G. Joshi, M. K. Okajima, T. Kaneko, *Adv. Mater. Interfaces* **2018**, *5*, 1701219.
[33] G. Joshi, K. Okeyoshi, T. Mitsumata, T. Kaneko, *J. Colloid Interface Sci.* **2019**, *546*, 184.
[34] I. Saito, L. Wu, M. Hara, Y. Ikemoto, T. Kaneko, K. Okeyoshi, et al. *ACS Appl. Polym. Mater.* **2022**, *4*, 7054.
[35] T. K. L. Nguyen, Y. Tonomura, N. Ito, A. Yamaji, G. Matsuba, M. Hara, Y. Ikemoto, K. Okeyoshi, et al. *Langmuir* **2024**, *40*, 11927.
[36] L. Wu, I. Saito, K. Hongo, K. Okeyoshi, *Adv. Mater. Interfaces* **2023**, *10*, 2300510.
[37] W. Thielicke, R. Sonntag, *J. Open Res. Softw.* **2021**, *9*.
[38] J. S. Hong, K. H. Ahn, G. Fuller, M. C. Kim, *Phys. Fluids* **2023**, *35*, 064103.

[39] S. Shin, J. T. Ault, K. Toda-Peters, A. Q. Shen, *Phys. Rev. Fluids* **2020**, *5*, 024304.
[40] K. Okeyoshi, M. Yamashita, K. Budpud, G. Joshi, T. Kaneko, *Adv. Mater. Interfaces* **2019**, *6*, 1900855.
[41] M. Rodríguez-Hakim, J. M. Barakat, X. Shi, E. S. Shaqfeh, G. G. Fuller, *Phys. Rev. Fluids* **2019**, *4*, 034002.
[42] J. S. Hong, K. H. Song, P. J. Daivis, M. C. Kim, *Phys. Fluids* **2024**, *36*, 084110.
[43] N. Gnan, E. Zaccarelli, *Nat. Phys.* **2019**, *15*, 683.
[44] P. G. de Gennes, F. Brochard-Wyart, D. Quéré, *Capillarity and Wetting Phenomena* Springer-Verlag, New York **2004**.
[45] P. Lambert, A. Delchambre, *Langmuir* **2005**, *21*, 9537.
[46] C. L. McTaggart, *J. Fluid Mech.* **1983**, *134*, 301.

Chapter 4

Convection, fluctuation, nucleation

4.1 Introduction

Evaporation-driven self-assembly has emerged as a powerful route for organizing soft matter systems, particularly within confined geometries such as Hele-Shaw cells.[1-3] In such systems, the interplay between evaporation, concentration gradients, and interfacial dynamics can give rise to complex pattern formation.[4] One striking manifestation is meniscus splitting,[5] where polymer molecules spontaneously accumulate and organize at the retreating air-liquid interface due to local concentration. Despite extensive studies on evaporation-induced deposition, the temporal and spatial dynamics of nucleation in these systems remain incompletely understood, especially synchronous and asynchronous nucleation process.[6-8] While systems lacking flow often exhibit uniform, temporally synchronized nucleation across the interface, systems with convection can display spatial heterogeneities and irregular timing in the appearance of nucleated domains.[9-11] However, the relationship between convection and nucleation has not been systematically explored in the meniscus splitting phenomenon with Marangoni circulation.

In this study, we investigate how evaporation-induced convective reorganization affects interfacial fluctuation and nucleation process at the interface (**Figure 4.1**). The synchronous and asynchronous nucleation was discussed in the case of pectin dispersion meniscus splitting. Also, the role of the bottom boundary in modifying convective symmetry and interfacial dynamics is discussed based on both symmetry breaking in convection and fluctuations at the interface. Finally, we compare two model systems: pectin, which promotes significant convection flow and xanthan gum, which exhibits minimal internal flow under evaporation. These contrasting behaviors provide a natural platform to examine how flow alters nucleation dynamics. The central question we pose is: How does internal convection, driven by evaporation, influence the temporal synchronization of nucleation during interfacial assembly? To answer this, we monitor the evolution of meniscus splitting and domain formation in Hele-Shaw geometries under

identical evaporation conditions, isolating the effects of fluid motion. By focusing on the distinction between synchronous and asynchronous nucleation, this work explores to deepen our understanding of far from equilibrium processes.

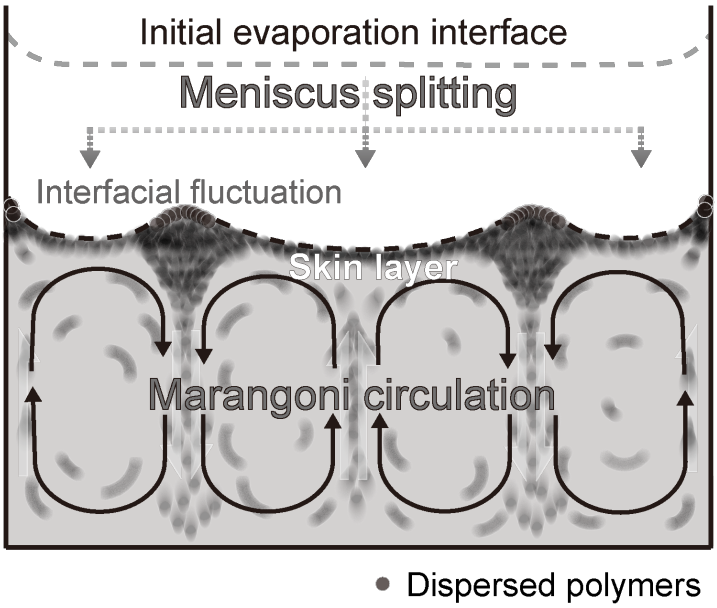

Figure 4.1 Schematic illustration of nucleation process in pectin dispersion through Marangoni circulation, the formation of the interfacial fluctuation and skin layer indicate pre-nucleation.

4.2 Experimental

4.2.1 Materials

Pectin (Mw = 20–400 kDa) obtained from citrus was purchased from Nacalai Tesque, Japan. Low-methoxy pectin contained more than 50% galacturonic acid units and 11% methoxy groups. Xanthan gum (Mw = 4.7×10^6 g·mol^{-1}) obtained from xanthomonas campestris, neosoft XC, was purchased from Taiyo Kagaku Co. Japan. The polysaccharides powder was dispersed in pure water at room temperature. The aqueous pectin dispersion was stored in a refrigerator and used within one week to prevent property changes. A polystyrene divinylbenzene copolymer microsphere suspension, purchased from Thermo Fisher Scientific, with a specific density of 1.05 g/cm^3, was used as a tracer particle. The mean diameter of the particles was 12 μm with a distribution coefficient of variation ≤18%. The suspension was dispersed in the prepared aqueous pectin dispersion after a brief (15 s) immersion in a low-power ultrasonic bath. The Hele-Shaw cell (X-width, Y-gap, and Z-depth) was composed of two nonmodified glass slides and U-shaped polyvinyl chloride spacers with the required thickness. Nonmodified glass substrates were purchased from Matsunami Glass Ind. Ltd., Japan.

4.2.2 Drying experiment

After removing minor amounts of impurities and air bubbles through centrifugation (6000 rpm, 15 s), the dispersion was filled in the top-open Hele-Shaw cell to avoid the deposition of tracer particles. The drying experiment was carried out in a drying observation box at a controlled temperature and atmospheric pressure maintained using an air circulator. During drying, the samples were monitored through glass windows and images were captured using a Canon EOS kiss X10.

4.2.3 Image analysis

Particle image velocimetry (PIV) analysis was performed on 8-bit images obtained during the drying experiment (10 min frame interval) using PIVlab in MATLAB. Before analysis, the image sequences were cropped into a region of interest to fit the size of Hele-

Shaw cells and preprocessed using the contrast-limited adaptive histogram equalization value of 64 pixel with auto contrast stretch. Image pairs (A–B and B–C) were cross-correlated to extract the local displacement between two frames based on the fast Fourier transforms (FFT) window deformation algorithm. The size of the interrogation area was 128×128 pixel, followed by two passes with half the step of the previous size. The last pass was repeated until the quality slope was < 0.025. A Gaussian 2×3 fit was used for the subpixel accuracy with high correlation robustness. The drying experiment was compiled into a video with a magnitude display and a suitable scale bar.

Interfacial behaviors were analyzed by image sequences in drying experiments using the ImageJ software (National Institutes of Health, Bethesda, MD, USA). A stack of images was obtained every 10 min to demonstrate the interfacial behavior under different conditions. The spatiotemporal analysis of the interfacial motion speed was performed by reslicing the image sequences of the given interfacial positions in the nucleation positions and center of the emerged meniscus during evaporation (M1, N1, M2, N2, and M3). The Z-position of the interface was plotted using a GetData Graph Digitizer. The interfacial speed (dZ/dt) was estimated using Z-position plots. The speed of the tracer particles was also manually extracted for careful analysis of the convection behavior in the outer loop regions. The path of particle motion was determined by stacking every 100 min (at 10 min intervals, 11 images), and the speed (dZ/dt) was plotted every 100 min.

4.3 Results and discussion

4.3.1 Synchronous and asynchronous nucleation in pectin dispersion

Through particle image velocimetry analysis, we investigated the internal flow dynamics of pectin dispersions undergoing evaporation in a Hele-Shaw cell, with particular attention to Marangoni convection patterns and their relationship to nucleation behavior at the air–liquid interface. Under otherwise similar experimental conditions, two distinct nucleation modes were observed: synchronous and asynchronous nucleation (**Figure 4.2**). In the synchronous nucleation, pectin particles at the air–liquid interface simultaneously formed two nucleation centers during evaporation. These centers emerged nearly simultaneously and symmetrically, accompanied by relatively balanced and symmetric Marangoni flow patterns. This suggests that under such flow conditions, surface tension gradients are evenly distributed, providing multiple favorable sites for localized concentration buildup and subsequent gel-like flocculation. In contrast, asynchronous nucleation was characterized by a sequential formation of two nucleation centers. Initially, pectin particles accumulated and flocculated at one site on the interface, forming a visible nucleus. Only after this initial event did a second nucleus form at a different position, once the local concentration reached a similar threshold, as the air-liquid interface shown after 30 h (**Figure 4.2a**). After nucleation, the evaporative interfaces become similar as shown at 100 h. PIV analysis revealed that this process was strongly associated with asymmetric Marangoni circulations. Specifically, the primary nucleus often corresponded with a region of stronger flow as the velocity field shown (**Figure 4.2b**), indicating that local enhancement of particle transport due to flow asymmetry may play a key role in initiating the first nucleation. These findings suggest that the balance or imbalance of internal convective flows governed by subtle differences in evaporation rate, concentration gradients, and cell geometry can regulate whether nucleation occurs simultaneously at multiple positions sequentially. Understanding the interplay between interfacial nucleation kinetics and internal fluid motion offers new

insight into controlling pattern formation in drying colloidal dispersions.

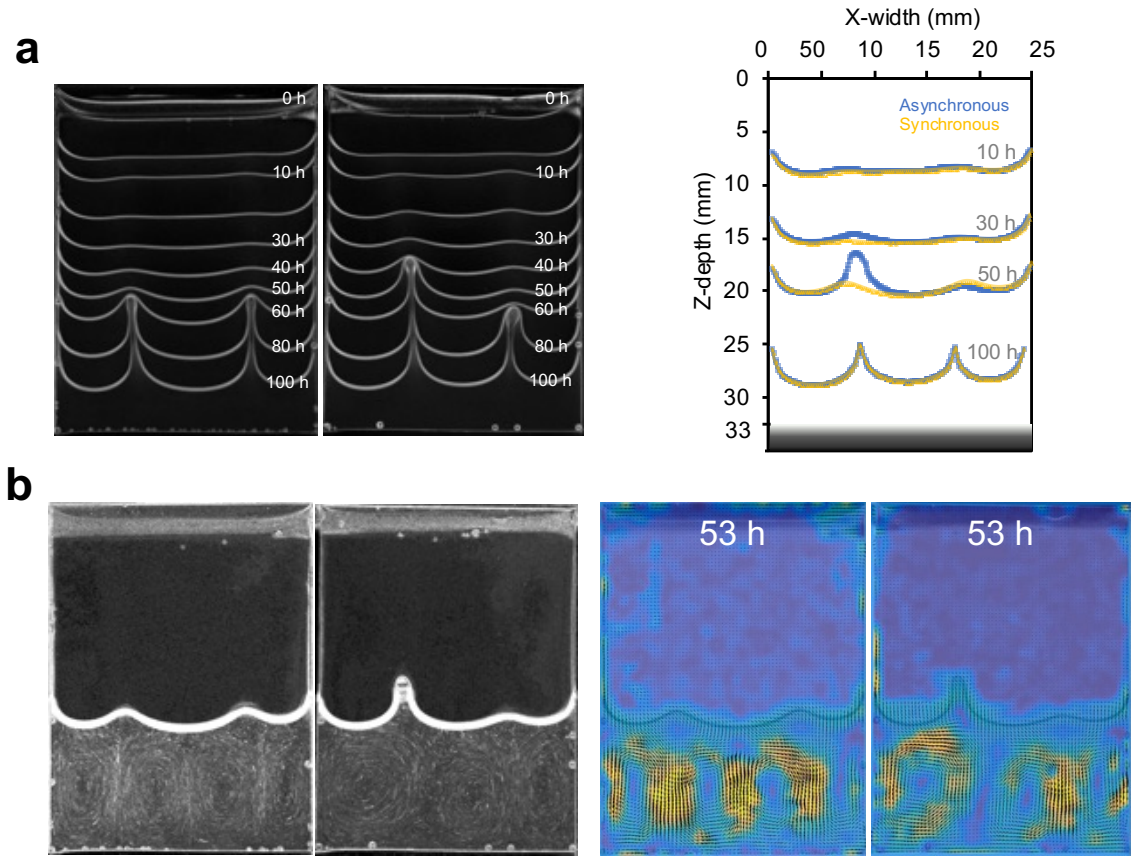

Figure 4.2 Synchronous and asynchronous nucleation in pectin dispersion. a) Stack images of synchronous and asynchronous nucleation process in pectin dispersions, drying temperature: 40 °C, C_0 of pectin dispersion = 6.0 wt%, cell size: (25 mm-width, 1 mm-gap, 33 mm-depth). The interface curves of synchronous and asynchronous nucleation process corresponding to time: 10 h, 30 h, 50 h, 100 h. **b)** The convection pattern in synchronous and asynchronous nucleation during 53–55 h, and the corresponding velocity field distributions at 53 h.

4.3.2 Convection patterns on interfacial nucleation

The convective differences that occur after synchronous and asynchronous nucleation have just been described. Despite similar conditions, there is a slight difference in the timing of the bottoming of the convective plumes, will inducing symmetry breaking. To controlled asymmetry, we used the Hele shaw cell with different shapes of bottom geometry as flat, step-like, and sloped bottoms (**Figure 4.3a**). Different from the flat-bottom in Figure 4.2, in the step-like bottom, the left plume touched the bottom at roughly 300 min, while the right plume was locally perturbed by the updraft fluid. So that by 1700 min only the left interface exhibited a pronounced fluctuation and subsequent flocculated nucleus, while the right side remained quiescent. In the sloped bottom, the continuous depth gradient produced staggered bottoming process: plumes merged into a single central fluctuation after sequential bottoming, ultimately yielding a nucleation position at mid-X-width in the cell. These results strongly indicated that the asymmetrical bottom caused the symmetry breaking of convection patterns, which affected the interfacial fluctuation and nucleation process during meniscus splitting. Under three different bottoms, the initial merging of the plumes leads to the formation of corresponding interface fluctuations. However, due to the different order of the plumes touch the bottom, the interface fluctuations are affected by convection. In the case of flat bottom, the two plumes touch the bottom at similar timing. the two plumes touch the bottom at similar times, forming symmetric convection circles, and the corresponding interface fluctuations stabilize and nucleate with evaporation. For a step-like bottom, the left plume reaches the bottom first, forming a circulation, while the right plume is disturbed, breaking the symmetry of convection; thus, only the interface fluctuations on the left stabilize and nucleate, while those on the right disappear. For a sloped bottom, the two converging plumes meet and interact in the middle, causing interface fluctuations to cluster at the center, leading to nucleation at the middle position. These observations underscore that geometric biases can cascade through convective circulations to break symmetry, thereby selecting the positions and chronology of interfacial instability. Specifically, the plume

that bottoms first establishes a dominant flow that impairs its counterpart, precipitating asynchronous or centralized nucleation. This result provides guidance that the emergence of nucleation in space and time can be guided by changing the boundary geometry rather than the concentration gradient.

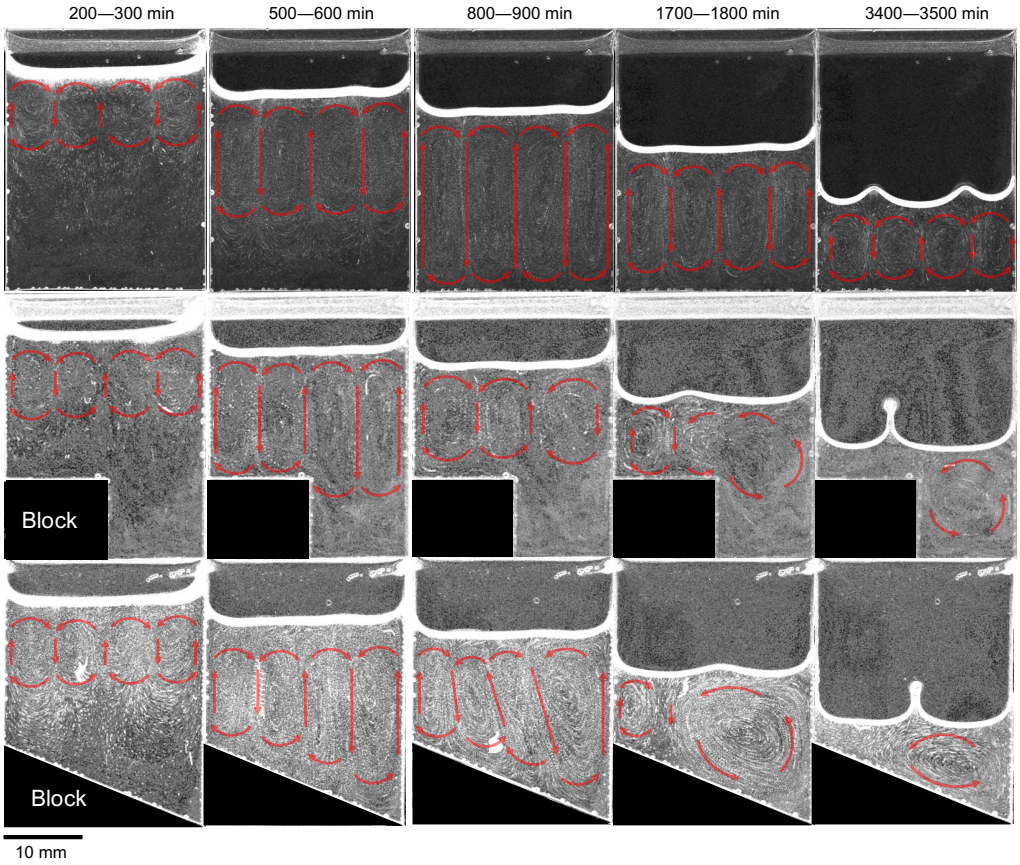

Figure 4.3 The convection patterns in the cells with flat, step-like and sloped bottoms at given times. Drying temperature: 40 °C, C_0 of pectin dispersion = 6.0 wt%, cell size: 25 mm-width, 1 mm-gap, 23mm on the left-depth 33 mm on the right-depth of the step-like and sloped bottoms. The red arrows show the flow direction.

4.3.3 Nucleation process with and without convection pattern

Surprisingly, convection was found to be nonessential for nucleation. By comparing the evaporation process of two different polysaccharide dispersions: pectin and xanthan gum. During the meniscus splitting of xanthan gum dispersion, interfacial fluctuations and nucleation occurred without internal convection. The spatiotemporal analysis of two polysaccharide dispersions was compared with tracer particles. As shown in **Figure 4.4a**, as the drying of the pectin dispersion with an initial concentration of 6.0 wt%, the Marangoni convection was emerged in the liquid phase. The time course image shows the meniscus splitting process with interfacial fluctuation, and nucleation. When the initial concentration was 4.5 wt%, the internal convection became asymmetrical, the nucleation position shifted significantly downward, and the time course of interface revealed a tendency for asynchronous nucleation after 30 h (with the second nucleus eventually not appearing). However, in the case of xanthan gum dispersion, the interfacial fluctuations occurred with evaporation, no significant circulation flow was observed (**Figure 4.4b**). As the initial concentration decreased from 1.5 wt% to 1.25 wt%, the nucleation changed from two nuclei splitting the interface to one nucleus splitting the interface, and the depth of nucleation remained nearly unchanged. The absence of internal Marangoni convection, as confirmed by PIV analysis, suggests that the surface tension gradients driving such flows were either negligible or efficiently suppressed in the xanthan system. A possible explanation lies in the physicochemical of xanthan gum: the molecular structure and high viscosity may inhibit the surface tension driven flow.[12] Although both pectin and xanthan gum possess abundant hydroxyl and carboxyl groups capable of forming hydrogen bonds, xanthan gum exhibits markedly different solution behavior due to its rigid, semi-helical backbone and branched side chains.[13] This structural rigidity promotes the formation of physical crosslink, which significantly limits molecular mobility. Therefore, internal convection is less likely to occur in xanthan gum dispersion during drying. We hypothesize that convection suppression confines solute redistribution to evaporation-driven accumulation. This concentration buildup along the

curved interface induces stress concentration, initiating nucleation. Furthermore, the yield-stress behavior of Xanthan gum may contribute to a quasi-solid interfacial environment that prevents redistribution of material.[14]

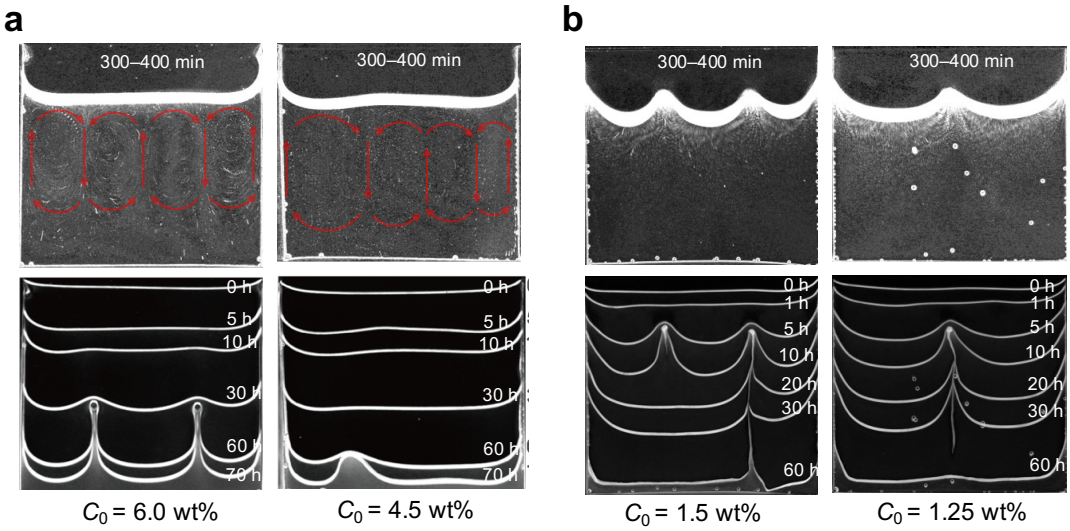

Figure 4.4 a) The stack images of drying pectin dispersions at 300-400 min and the time course image of the evaporation process. The stack images show the convection pattern during evaporation. Drying temperature: 40 °C, initial concentration: 6.0 wt%; 4.5 wt% , cell size: 25 mm-width, 1 mm-gap, 23mm-depth. **b)** The stack images of drying xanthan gum dispersions at 300-400 min and the time course of drying xanthan gum dispersion. The stack images show interfacial nucleation without internal convection patterns. The time course image shows the meniscus splitting process with interfacial fluctuation, and nucleation. Drying temperature: 40 °C, initial concentration: 1.5 wt%; 1.25 wt% , cell size: 25 mm-width, 1 mm-gap, 23mm-depth.

4.4 Conclusion

In this work, we compare the synchronous and asynchronous nucleation in pectin dispersion. The difference in the timing of the bottoming of the convective plumes may lead to symmetry breaking in the convection pattern. We have shown that the relative timing of convective plume bottoming governs interfacial nucleation during meniscus splitting: in a flat-bottom cell, symmetric plume contact yields simultaneous flows and synchronous nucleation, whereas simple geometric biases (step-like or sloped bottoms) stagger bottoming, break the convective symmetry, and localize nucleation to predictable positions. However, in the dispersion where Marangoni circulations are difficult to induce (e.g., xanthan gum dispersion), the nucleation process tends to occur synchronously. This behavior is closely related to the rigid chain structure and hydrogen bonds of xanthan gum dispersion. By linking bottom-touched dynamics to interfacial fluctuation, our work unveils a straightforward strategy to engineer spatially and temporally precise nucleation patterns—an insight of broad relevance to microfluidic design and precision coating technologies. This principle offers a versatile design handle for microfluidic patterning, precision coatings, and capillary-driven assembly in soft matter system. Unraveling these mechanisms is essential not only for advancing fundamental soft matter physics,[15] but also for guiding the design of controlled deposition strategies in material fabrication and bio-inspired patterning.[16,17]

References

[1] J. Sui, *Phys. Fluids*, **33** (2021).

[2] R. Iqbal, A. Matsumoto, D. Carlson, K. T. Peters, R. Funari, A. K. Sen, & A. Q. Shen, *J. Colloid Interface Sci.*, 623, 927 (2022).

[3] B. Abedi, R. M. Oliveira, L. S. Berghe, , & P. R. de Souza Mendes, *Phys. Fluids*, **36** (2024).

[4] C.Kaplan, N. Wu, S.Mandre, J.Aizenberg, & L. Mahadevan, *Phys. Fluids*, **27** (2015).

[5] K. Okeyoshi, *Polym. J.*, **52**, 1185 (2020).

[6] M. Li, A.Wu, L. Li, Z. Li & H. Zang, *ACS Biomater Sci Eng*, **10**, 863 (2024).

[7] Z. Xun, G. He, Y. Huang, & R. Yu, *ACS Appl. Polym. Mater.*, **4**, 4949 (2022).

[8] P. G. Siddheshwar, B. S. Bhadauria, & O. P. Suthar, *Int. J. NonLin. Mech.*, **49**, 84 (2013).

[9] A. Chatterjee, N. Mears, Y. Yadati, & G. S. Iannacchione, *Entropy*, **22**, 561 (2020).

[10] K. Okeyoshi, M. K. Okajima, T. Kaneko, *Sci. Rep.*, **7**, 5615 (2017).

[11] L. Wu, I. Saito, K. Hongo, K. Okeyoshi, *Adv. Mater. Interfaces*, **10**, 2300510 (2023).

[12] G. Joshi, K. Okeyoshi, T. Mitsumata, & T. Kaneko, *J. Colloid Interface Sci.*, *546*, 184-191 (2019).

[13] E. M. Nsengiyumva, P. Alexandridis, *Int. J. Biol. Macromol.*, **216**, 583-604 (2022).

[14] K. Chalah, D. Hammiche, I. Bennnoui, & A. Benmounah, *Macromol. Res.*, **33**, 423-437. (2025).

[15] D. Qiao, W. Hu, Z. Wang, F. Xie, B. Zhang, & F. Jiang, *J. Food Eng.*, **360**, 111703 (2024).

[16] S. R. Ede, H. Yu, C. H. Sung, & D. Kisailus, *Small Methods*, **8**, 2301227 (2024).

[17] Y. Wang, G. Zheng, N. Jiang, G. Ying, Y. Li, X. Cai,... & X. Zhang, *Nat. Rev. Methods Primers*, **3**, 68 (2023).

Chapter 5

General Conclusion

5.1 Summary

This thesis investigates the meniscus splitting phenomenon in drying polysaccharide dispersions, focusing on the interfacial and inter-fluid self-organization mechanisms. Especially, the kinetic mechanism before nucleation of polymer particles. Overall, based on the spatiotemporal analysis, the goal of this work is to understand the unique integration of polymers during the nonequilibrium period of evaporation.

In Chapter 2, we demonstrated the importance of spatial finiteness at the evaporative interface. By applying heat to polymer dispersions, interface fluctuations lead to concentration unevenness, causing the meniscus to split. The asynchronous nucleation, observed in polysaccharide dispersions, highlights the role of nonequilibrium drying processes in driving the formation of multiple nuclei.

In Chapter 3, we investigated the internal liquid behavior during the evaporation process, revealing the significance of Marangoni circulations in shaping the polymer particles in skin layer formation. These circulations align with the nucleation positions, suggesting that they play a key role in the reordering of polymer clusters in the finite space of the meniscus, contributing to the periodic integration of polymers and the emergence of ordered patterns.

In Chapter 4, we discussed the relationship between the internal flow, fluctuation, and nucleation. In pectin dispersions, both synchronous and asynchronous nucleation were observed, with the latter closely linked to asymmetric Marangoni convection, which directed particles and determined the nucleation position. Conversely, xanthan gum dispersions exhibited no internal convection and consistently underwent synchronous nucleation, likely due to their high viscosity and viscoelastic properties suppressing internal flow. These contrasting behaviors underscore the pivotal role of rheological properties in regulating flow-driven phase organization during evaporation.

The findings in this work shed light on the broader implications for fields such as fluid dynamics, polymer science, and materials engineering, where self-organization

plays a crucial role in pattern formation at the micro- and nanoscale. This research provides a deeper understanding of the physical mechanisms that govern self-organizing patterns in nonequilibrium systems and offers valuable insights for developing technologies that harness these phenomena.

5.2 Future over

This study advances the understanding of the mechanism of meniscus splitting phenomenon. But there remain several problems for further research and exploration. One potential direction is to investigate the impact of different types of polymers and their molecular weight on the meniscus splitting behavior. Especially the complex polymers such as liquid crystal polysaccharide Xanthan gum, which showed unique fluid behavior during evaporation. Since the polymer's properties significantly influence the evaporation dynamics and interface interactions, exploring a broader range of polymers could offer a deeper understanding of the universal mechanisms that govern pattern formation.

From a theoretical perspective, due to the complex mechanisms of both convective and non-convective behaviors, theoretical studies by computer simulations have become quite challenging. Future research should focus on thermodynamic analysis to establish macroscopic models. By applying the principles of nonequilibrium thermodynamics and self-organization, future studies could refine models to predict pattern outcomes under different conditions, potentially enabling the design of advanced materials with tailored properties for use in fields such as sensors, drug delivery systems, and nanotechnology.

From an application perspective, different basic polymers show varying oriented properties in meniscus splitting, with polysaccharides displaying distinct behaviors. By incorporating the fluid properties of different microparticles, such as shape, thermal sensitivity, and ion responsiveness, the potential for enhancing meniscus splitting behavior is greatly expanded, offering exciting possibilities for advanced applications.

Furthermore, the exploration of the interaction between fluid flows and phase transitions could be a promising area of research. Understanding how the balance between liquid evaporation and solidification influences the evolving patterns could have implications for materials design, particularly in the development of responsive coatings and microfluidic devices.

List of publications

Journal (Peer-reviewed):

- I. Saito, L. Wu, M. Hara, Y. Ikemoto, T. Kaneko, & K. Okeyoshi, Anisotropic responses with cation selectivity in hierarchically ordered polysaccharide networks. *ACS Appl. Polym. Mater.*, **4**, 7054 (2022).

- L. Wu, I. Saito, K. Hongo, & K. Okeyoshi, Recognition of Spatial Finiteness in Meniscus Splitting Based on Evaporative Interface Fluctuations. *Adv. Mater. Interfaces*, **10**, 2300510 (2023).

- L. Wu, K. Okeyoshi, et al. Nonequilibrium Period with Emergence of Marangoni Circulations in Meniscus Splitting, submitted.

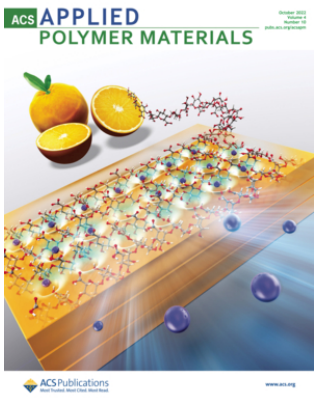

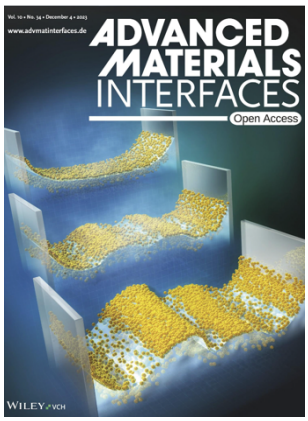

International Conference:

- L. Wu, I. Saito, K. Hongo, K. Okeyoshi. "Interfacial fluctuation in binucleation of meniscus splitting on pectin aqueous dispersion" *2022 MRS Fall Meeting*, online, December 2022, Oral.
- L. Wu, K. Okeyoshi. "Quasi-Two-dimensional Marangoni Convection and Specific Polymer Deposition in Meniscus Splitting Phenomenon" *2024 MRS Spring Meeting & Exhibit,* Seattle, April 2024, Oral.
- L. Wu, K. Okeyoshi. "Convective Self-assembly of Polysaccharide Particles in Meniscus Splitting". *2024 Gel symposium,* Okinawa, November 2024, Poster.
- L. Wu, K. Okeyoshi. "Convective Self-assembly of Polysaccharide Particles in Meniscus Splitting". *International Symposium on Exponential Biomedical DX 2024,*

Ishikawa, November 2024, Poster.

Domestic Conference:

- L. Wu, I. Saito, K. Hongo, K. Okeyoshi. “Interfacial fluctuation of meniscus splitting using polysaccharide aqueous dispersion”. *The 1st Symposium on Molecular Life Reactions, FOREST,* Kanazawa, February 2023, (Poster).
- L. Wu, K. Okeyoshi. “Specific polymer deposition in meniscus splitting and the effect of Marangoni convection” *The 72nd Symposium on Macromolecules, SPSJ,* Kagawa, September 2023, Oral.
- L. Wu, K. Okeyoshi. “Emergence of Quasi-Two-Dimensional Convection and Reposition of Polymer Particles in Meniscus Splitting”. *The 73rd SPSJ Annual Meeting*, Sendai, June 2024, Poster.
- L. Wu, K. Okeyoshi. “Topological Reorganization of Polymer Particles in Meniscus Splitting through Convective Assembly”. *The 73rd Symposium on Macromolecules, SPSJ,* Niigata, September 2024, Oral.

Other works during Master program (2020.10-2022.9):

Conference:

- L. Wu, I. Saito, K. Hongo, K. Okeyoshi. “Interfacial fluctuation on meniscus splitting and preparation of polysaccharide gels in microdevice” *The 33rd Symposium on Polymer Gels,* online, January 2022, Oral.
- L. Wu, I. Saito, K. Hongo, K. Okeyoshi. “Interfacial Fluctuation of Meniscus Splitting Using Polysaccharide Aqueous Dispersion as Viscous Fluids” *2022 Gel symposium,* Hokkaido, September 2022, Poster.
- L. Wu, I. Saito, K. Hongo, K. Okeyoshi. “Interfacial fluctuation in meniscus splitting pattern formation and preparation of polysaccharide-oriented gels” *The 71st Symposium on Macromolecules, SPSJ,* Hokkaido, September 2022, Oral.